

1 **High resolution vertical distribution and sources of HONO and NO₂ in the**
2 **nocturnal boundary layer in urban Beijing, China**

3
4 **Fanhao Meng^{1,2}, Min Qin¹, Ke Tang^{1,2}, Jun Duan¹, Wu Fang¹, Shuaixi Liang^{1,2}, Kaidi Ye^{1,2},**
5 **Pinhua Xie^{1,2,3,5}, Yele Sun^{3,4,5}, Conghui Xie⁴, Chunxiang Ye⁶, Pingqing Fu^{4,*}, Jianguo Liu^{1,2,3},**
6 **Wenqing Liu^{1,2,3}**

7 ¹Key Laboratory of Environmental Optics and Technology, Anhui Institute of Optics and Fine
8 Mechanics, Chinese Academy of Sciences, Hefei, 230031, China

9 ²University of Science and Technology of China, Hefei, 230027, China

10 ³Center for Excellence in Regional Atmospheric Environment, Institute of Urban Environment,
11 Chinese Academy of Sciences, Xiamen, 361021, China

12 ⁴State Key Laboratory of Atmospheric Boundary Layer Physics and Atmospheric Chemistry, Institute
13 of Atmospheric Physics, Chinese Academy of Sciences, Beijing, 100029, China

14 ⁵University of Chinese Academy of Sciences, Beijing, 100049, China

15 ⁶State Key Joint Laboratory of Environmental Simulation and Pollution Control, College of
16 Environmental Sciences and Engineering, Peking University, Beijing, China

17 *now at: Institute of Surface-Earth System Science, Tianjing University, Tianjing, 300072, China

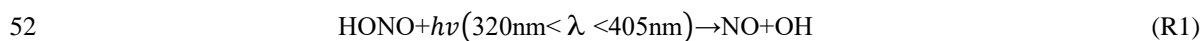
18 **Correspondence:** Min Qin (mqin@aiofm.ac.cn)

19
20 **Abstract.** Nitrous acid (HONO), an important precursor of the hydroxyl radical (OH), plays a key role
21 in atmospheric chemistry, but its sources are still debated. The production of HONO on aerosol surface
22 or on ground surface in nocturnal atmospheres remains controversial. The vertical profile provides
23 vertical information on HONO and NO₂ to understand the nocturnal HONO production and loss. In this
24 study, we report the first high-resolution (<2.5 m) nocturnal vertical profiles of HONO and NO₂
25 measured from in-suit instruments on a movable container that was lifted on the side wiring of a 325-m
26 meteorological tower in Beijing, China. High-resolution vertical profiles revealed the negative
27 gradients of HONO and NO₂ in nocturnal boundary layers, and a shallow inversion layer affected the
28 vertical distribution of HONO. The vertical distribution of HONO was consistent with stratification and
29 layering in the nocturnal urban atmosphere below 250 m. The increase of HONO/NO₂ ratio was
30 observed throughout the column from the clean episode to the haze episode, and a relatively constant

31 HONO/NO₂ ratios in the residual layer were observed during the haze episode. Direct HONO
32 emissions from traffic contributed 29.3% ± 12.4% to the ambient HONO concentrations at night. The
33 ground surface dominates HONO production by heterogeneous uptake of NO₂ during the clean episode.
34 In contrast, the HONO production solely on aerosols (30–300 ppt) explained the observed HONO
35 increases (15–368 ppt) in the residual layer, suggesting that the aerosol surface was the location where
36 the HONO was formed, which could presumably dominate the production of HONO aloft during the
37 haze episode. Average dry deposition rates of 0.74 ± 0.31 and 1.55 ± 0.32 ppb h⁻¹ were estimated
38 during the clean and haze episodes, implying that significant quantities of HONO could be deposited to
39 the ground surface at night. Our results highlight ever-changing contributions of aerosol and ground
40 surfaces in nocturnal HONO production at different pollution levels and encourage more vertical
41 gradient observations to evaluate the contributions from varied HONO sources.

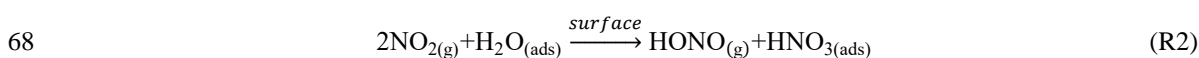
42 **1 Introduction**

43 It is well known that the rapid photolysis of nitrous acid (HONO) (R1) after sunrise is the most
44 important hydroxyl radical (OH) source. 25%–60% of daytime OH production was accounted for due
45 to HONO photolysis, according to previously reported (Lu et al., 2012; Ma et al., 2017; Tong et al.,
46 2016; Su et al., 2008b; Huang et al., 2017; Spataro et al., 2013). OH initiates daytime photochemistry
47 and promotes the formation of secondary products (including ozone (O₃) and peroxyacetyl nitrate
48 (PAN)) and secondary aerosols (Alicke and Platt, 2002; Tang et al., 2015; Kleffmann, 2007; An et al.,
49 2012). In addition, HONO as a nitrosating agent forms carcinogenic nitrosamines (Sleiman et al., 2010;
50 Bartolomei et al., 2015; Gómez Alvarez et al., 2014), and its health effects have attracted increasing
51 amounts of concern (Hanst et al., 1977; Pitts et al., 1978).



53 Despite the importance of HONO, the details of the formation processes of HONO in the
54 atmosphere are debated for decades. New state-of-the-art science instruments have observed much
55 higher daytime HONO concentrations than simulated values from atmospheric chemical models in both
56 rural and urban areas, implying missing HONO sources (Li et al., 2012; Wang et al., 2017; Oswald et
57 al., 2015; Wong et al., 2012; Li et al., 2014; Liu et al., 2019; Karamchandani et al., 2015; Kleffmann,
58 2007; Mendez et al., 2017; Michoud et al., 2014; Michoud et al., 2015; Tang et al., 2015; Vogela et al.,
59 2003; Sörgel et al., 2011). Several homogeneous reaction mechanisms for HONO have been proposed,

60 but the latter have been considered as irrelevant under actual atmospheric conditions, including
61 photolysis of ortho-substituted nitroaromatics (Bejan et al., 2006) and the reaction of photoexcited NO₂
62 with H₂O (Li et al., 2008). The heterogeneous reduction of NO₂ with organic substrates is proposed to
63 be another effective pathway to generate HONO (Brigante et al., 2008; Stemmler et al., 2006; George
64 et al., 2005). However, extrapolation of lab results to real surfaces remains challenging. The nocturnal
65 production of HONO has been considered to be dominated by the NO₂ heterogeneous reaction (R2).
66 Although the heterogeneous reaction (R2) of HONO formation is first-order in NO₂, the mechanism for
67 the conversion of NO₂ on surfaces remains unclear (Finlayson-Pitts et al., 2003; Finlayson-Pitts, 2009).



69 A few studies have evaluated the relative importance of aerosol and ground surfaces in the
70 nocturnal production of HONO via reaction (R2). The heterogeneous reaction on ground surface have
71 been suggested as the primary nocturnal HONO source based on vertical measurements and fluxes in
72 HONO (Harrison and Kitto, 1994; Harrison et al., 1996; Laufs et al., 2017; Kleffmann et al., 2003; Su
73 et al., 2008b; VandenBoer et al., 2013; Villena et al., 2011; Wong et al., 2011; Wong et al., 2013; Stutz
74 et al., 2002; Ye et al., 2017; Zhang et al., 2009). However, other ground level studies have found
75 significantly positive correlations between HONO/NO₂ and aerosol surface areas, which suggests that
76 the aerosols play an important role in the heterogeneous conversion of NO₂ to HONO (Reisinger, 2000;
77 Cui et al., 2018; Zhang et al., 2018; Hou et al., 2016; Tong et al., 2016; An et al., 2012; Bao et al., 2018;
78 Liu et al., 2014; Reisinger, 2000). Therefore, the primary reaction surfaces for the nighttime HONO
79 formation is still controversial, and the role of the aerosols in the heterogeneous production of HONO
80 remains an open question.

81 Vertical gradient observations provide evidence regarding surfaces and in situ HONO formation,
82 which can help to understand the nighttime HONO sources. Methods of long-path differential optical
83 absorption spectroscopy (LP-DOAS) (Stutz et al., 2002; Wong et al., 2011; Wong et al., 2012),
84 instruments mounted on a movable elevator of a tall tower or a fixed height on a building (Kleffmann
85 et al., 2003; VandenBoer et al., 2013; Villena et al., 2011) and aircraft measurements (Zhang et al.,
86 2009; Li et al., 2014; Ye et al., 2018) have been applied for HONO vertical gradient observations in
87 Europe and the America. To determine the surface responsible for nocturnal HONO formation,
88 Kleffmann et al. (2003) and Wong et al. (2011) measured the HONO vertical gradient between 10 and

89 190 m altitude in a semi-rural area in Germany and at three different height intervals (lower: 20–70 m,
90 middle: 70–130 m and upper: 130–300 m) in downtown Houston. Their consistent conclusion was that
91 the reaction on the ground surfaces dominated the nocturnal formation of HONO. However, these types
92 of measurements are limited by the measurement frequency or vertical resolution between the surface
93 and the planetary boundary layer (PBL). VandenBoer et al. (2013) performed measurements of high
94 resolution vertical profiles (vertical resolution ~10 m) of HONO on a 300-m tower. The total column
95 observations of HONO also showed the ground as the dominant nocturnal surface on which HONO
96 was generated from the heterogeneous reaction of NO₂. The vertical information of HONO were
97 interpreted in conjunction with a chemical model. The results suggested a conservative surface
98 reservoir that was formed by the deposition of HONO could be a significant fraction of the unknown
99 daytime source. Furthermore, in an attempt to understand the importance of HONO photochemistry in
100 the troposphere, HONO gradients were measured in the PBL and the lower free troposphere (FT) over
101 a forested region in Michigan (Zhang et al., 2009). An evaluation of the relative importance of aerosol
102 and ground surfaces for the heterogeneous production of HONO also suggested that the ground surface
103 was a major HONO source in the lower boundary layer. In addition, a substantial amount of daytime
104 HONO existed in the FT (~8 ppt).

105 Beijing, as the largest and the most densely populated city in China, has suffered from severe haze
106 pollution for several years due to rapid economic development and urbanization. Several ground-based
107 observations of HONO have been conducted in urban and suburban areas of Beijing in recent years
108 (Tong et al., 2016; Zhang et al., 2018; Hou et al., 2016; Wang et al., 2017; Lu et al., 2012; Hendrick et
109 al., 2014). Higher levels of HONO have been observed (up to 9.71 ppb) in Beijing during winter
110 (Spataro et al., 2013). Although few near real-time HONO vertical gradients have been made, and they
111 have suggested that the reaction at the ground surface is the most important nighttime HONO source
112 (Kleffmann et al., 2003; VandenBoer et al., 2013; Wong et al., 2012; Zhang et al., 2009). The relative
113 importance of aerosol and ground surface in the production of nocturnal HONO may be different in the
114 Beijing region. First, as the primary precursor of nighttime HONO, NO₂ has a much higher
115 concentration during winter in Beijing due to the burning of fossil fuels and vehicle emissions. Second,
116 the aerosol surface area has been reported to be two to three orders of magnitude higher than the typical
117 background area (Cai et al., 2017; Liu et al., 2012; Zhang et al., 2015). High aerosol surface area levels
118 favor heterogeneous reactions on aerosol surfaces (haze period: 3000 μm² cm⁻³; Wang et al., 2018),

119 which presumably makes aerosol surfaces to play a more important role in the production of nighttime
120 HONO. Third, there is more stable nocturnal stratification during the haze period in winter in Beijing,
121 which may have influenced the vertical distribution of HONO. The contribution of the surface
122 production of HONO to HONO levels aloft may be overestimated.

123 In this study, the first high-resolution vertical profile measurements of HONO and NO₂ in the
124 megacity of Beijing at different pollution levels (following the transition from a clean episode to a haze
125 episode) are reported. The vertical profiles of HONO and NO₂ are measured at high vertical resolution
126 (< 2.5 m over 240 m height) between the surface, the nocturnal boundary layer, and the residual layer.
127 Although the vertical profile measurements are rather limited in scope, including only four nights in
128 December 2016, with limited ancillary data, this study is unique due to the high vertical resolution
129 obtained and due to the continuous HONO and NO₂ vertical measurements obtained at different stages
130 of pollution. The vertical profiles are then interpreted to evaluate the aerosol and ground surfaces
131 responsible for the nighttime HONO formation during different pollution periods. The vertical
132 measurements and simultaneous observations at ground level are then used to identify and quantify
133 nighttime HONO sources.

134 **2 Experimental Methods**

135 **2.1 Measurement site**

136 Vertical profile measurements were conducted from December 7th to 12th of 2016 at the Tower
137 Branch of the Institute of Atmospheric Physics (IAP), Chinese Academy of Science (39°58'N,
138 116°23'E) as part of the “In-depth study of air pollution sources and processes within Beijing and its
139 surrounding region (APHH-Beijing)” winter campaign. The site is a typical urban residential area
140 located between the 3rd and 4th Ring Road in the north of Beijing. It is approximately 1 km from the 3rd
141 Ring Road, 200 m from the Beijing-Tibet Expressway, and 50 m from the Beitucheng West Road (Fig.
142 S1). The primary sampling platform was the Beijing 325-m meteorological tower (BMT), equipped
143 with an external container that was lifted on the side wiring of the tower, which could ascend and
144 descend at a relatively constant rate of ~ 9 m min⁻¹. A single vertical ascent or descent required less
145 than 30 min. After reaching the top, the container stopped and data were measured continuously for 5–
146 20 min of each cycle. For security reasons, the container reached a maximum height limit of 260 m
147 during the daytime and 240 m at night (Fig. 1). The container instruments included the following: a

148 global position system (GPS), an altimeter, and an incoherent broadband cavity enhanced absorption
149 spectrometer (IBBCEAS) for measurements of HONO and NO₂. In addition, another IBBCEAS was
150 mounted in temperature-stabilized lab containers for the measurement of HONO and NO₂ at ground
151 level.

152 **2.2 Instrumentation**

153 HONO and NO₂ were simultaneously measured using a home-made IBBCEAS. A detailed
154 description of the IBBCEAS instrument can refer to Duan et al (2018), and its application to the
155 measurement made during this study is described below. IBBCEAS is a spectroscopic technique that
156 combines broad-band light source (UV-LED) with the principle of time-integrated cavity output
157 spectroscopy. The HONO was sampled into an inlet tube (1.5 m length with a 4 mm outside diameter
158 (OD)) before entering an optical cavity (550 mm in length and 25.4 mm OD) that utilized PFA to
159 minimize the HONO loss. The sampling gas flow rate was controlled at six standard liters per minute
160 (SLPM) by a gas pump (KNF). In the optical cavity, light was reflected between the two highly
161 reflective mirrors (R = 99.980% @368 nm, CRD Optics, California, USA) to obtain a long optical
162 absorption length. To protect the highly reflective mirrors, pure N₂ was used to continuously purge the
163 mirrors to prevent contact between the mirrors and the sample airflow. The purge flow rate was
164 controlled at 0.1 SLPM using mass flow controllers (MFCs, CS200A, Sevenstar, Beijing, China). The
165 typical time resolution of the IBBCEAS instrument was 30 s, and the 1 σ detection limits for HONO
166 and NO₂ were 90 ppt and 170 ppt, respectively. In this study, the IBBCEAS instrument was mounted in
167 a movable container of the BMT for vertical profile measurements, and this made measurements with a
168 time resolution of 15 s (vertical resolution of 2.4 m). The detection limits for HONO and NO₂ were 120
169 ppt and 200 ppt, respectively. Another IBBCEAS instrument was mounted in temperature-stabilized lab
170 containers at ground level, and it collected data with a time resolution of 30 s. The total relative
171 uncertainty of the IBBCEAS instrument was 8.7%, and it considered the uncertainty in the cross
172 section (5%), the calibration of reflectivity (5%), spectral fitting (4%), the effective cavity length (3%),
173 the pressure in the cavity (1%), $\Delta I/I_0$ (1%), and sample loss (0.5%). Correction of the light intensity
174 was performed every hour, and the mirror reflectivity was calibrated daily.

175 Meteorological parameters that included wind speed (WS), wind direction (WD), temperature (*T*),
176 and relative humidity (RH) were obtained using a 15-level meteorological gradient observation system

177 installed at fixed intervals along the meteorological tower (at heights of 8, 15, 32, 47, 65, 80, 100, 120,
178 140, 160, 180, 200, 240, 280, and 320 m). The gaseous species, including nitrogen monoxide (NO),
179 ozone (O₃), and carbon monoxide (CO) were measured using a commercial gas analyzer from Thermo
180 Scientific (Waltham, Massachusetts, USA) (Tan et al., 2017). NO was detected using NO-O₃
181 chemiluminescence (Model 42iTL, Thermo Scientific), with a detection limit of 50 ppt. O₃ and CO
182 were measured by an O₃ analyzer (Model 49i, Thermo Scientific) and a CO analyzer (Model 48iTLE,
183 Thermo Scientific), with the detection limits of 0.50 ppb and 0.04 ppm, respectively. Measurements of
184 NO, O₃ and CO agreed well within the instrumental accuracies. The 7-wavelength aethalometer (AE33,
185 Magee Scientific Corp, Berkeley, California, USA) was deployed to measure the black carbon (BC) at
186 a time resolution of 1 min (Xie et al., 2019). Aerosol particles were continuously collected onto a
187 quartz filter in the instrument to measure their light attenuation at 370, 470, 520, 590, 660, 880, and
188 950 nm. Trace gas (CO and O₃) and aerosol parameters (BC, NR-PM₁ and aerosol surface area) were
189 measured simultaneously at ground level and at 260 m on the tower. The non-refractory submicron
190 aerosol (NR-PM₁) species were measured simultaneously at ground level and at 260 m using an
191 aerodyne high-resolution time-of-flight aerosol mass spectrometer (AMS) and an aerosol chemical
192 speciation monitor (ACSM), respectively. The detailed sampling setup and calibration of the AMS and
193 ACMS, as well as data analysis, have been described by Xu et al. (2019) and Sun et al. (2013). The
194 dry-state particle number size distributions were measured at ground level and at 260 m using a
195 scanning mobility particle sizer (SMPS) (Du et al., 2017). The particle number size distributions of
196 15-500 nm was used to calculate the aerosol surface area (S_a) by assuming the particles are in spherical
197 shape. A hygroscopic factor $f(RH)$ was applied to correct S_a to the aerosol surface area in the real
198 atmosphere (S_{aw}) (Li et al., 2012). The S_{aw} was calculated using following equations:

$$199 \quad f(RH) = 1 + a \left(\frac{RH}{100} \right)^b \quad (1)$$

$$200 \quad S_{aw} = S_a \times f(RH) \quad (2)$$

201 where a and b are the empirical parameters used to estimate $f(RH)$, which were set to 2.06 and 3.6,
202 respectively (Liu et al., 2008). The uncertainty of S_{aw} was estimated to be ~30%, which was associated
203 with the uncertainty from the S_a measurement (~20%) and the growth factor (~20%).

204 **2.3 Inter-comparison**

205 In the present study, the measurements of HONO and NO₂ were conducted simultaneously in the

206 container and at ground level. Therefore, the calibration and inter-comparison of the two IBBCEAS
207 instruments were crucial. Comparison experiments were conducted in a temperature-stabilized
208 laboratory. The sampling unit and sampling flow rate of the two instruments were identical to minimize
209 measured deviations. Figure. 2 shows the excellent agreement between the two IBBCEAS instruments
210 (HONO: $R^2 = 0.99$, NO_2 : $R^2 = 0.99$), with a slope of 1.00 ± 0.01 (NO_2), 1.02 ± 0.01 (HONO) and a
211 small intercept of 180 ± 90 ppt (NO_2) and -30 ± 10 ppt (HONO). The difference was approximately 2%,
212 within the measurement error range of the instruments.

213 To verify the accuracy of the IBBCEAS instrument, an inter-comparison between the IBBCEAS
214 of this study and the IBBCEAS of Cambridge University was conducted. The HONO measurements
215 from the two different instruments were highly consistent ($R^2 = 0.97$, Fig. 2c), with a small intercept
216 and a slope close to 1. In addition, the IBBCEAS instrument was also compared with the long optical
217 path absorption photometer (LOPAP) and the stripping coil ion chromatography (SC-IC) from our
218 previous studies (Tang et al., 2019; Duan et al., 2018). This also showed good agreements of the HONO
219 measurements (LOPAP: $R^2 = 0.894$, SC-IC: $R^2 = 0.98$).

220 **3 Results and discussion**

221 **3.1 General observations and vertical measurements**

222 The time-series of meteorological parameters, trace gases, and aerosol parameters are shown in
223 Fig. 3. Based on the NR- PM_{10} mass concentration level, three different meteorological conditions were
224 characterized during the measurement periods (Table 1). The first episode (E1) from December 7th to
225 10:00 on December 8th was a haze event. The NR- PM_{10} mass concentration increased rapidly from 30 to
226 $\sim 150 \mu\text{g}\cdot\text{m}^{-3}$ at ground level and at 260 m on the tower due to a low wind speed ($0.78 \pm 0.42 \text{ m}\cdot\text{s}^{-1}$) and
227 a high RH ($51\% \pm 13\%$).

228 The second episode (December 8-11, C2) was a clean event with low NR- PM_{10} mass loading
229 (mean: $24 \pm 19 \mu\text{g}\cdot\text{m}^{-3}$) and a high wind speed ($> 5 \text{ m}\cdot\text{s}^{-1}$), primarily from northwest. The third episode
230 (E3) from December 11th to December 12th was another haze event. During this period, the atmosphere
231 was characterized by stagnant weather, lower wind speeds (an average of $0.77 \pm 0.4 \text{ m}\cdot\text{s}^{-1}$) and a high
232 RH ($55\% \pm 5\%$). The mass concentration of the NR- PM_{10} gradually increased and then remained at
233 relatively constant levels at ground level and 260 m on the tower, and ranging from 69 to $218 \mu\text{g}\cdot\text{m}^{-3}$
234 with a mean value of $154 \pm 35 \mu\text{g}\cdot\text{m}^{-3}$.

235 Throughout the entire measurement periods, HONO concentrations ranged from 0.05 to 7.59 ppb.
236 The mean HONO mixing ratios during E1, C2, and E3 were 4.26 ± 2.08 , 0.83 ± 0.65 , and 3.54 ± 0.91
237 ppb, respectively. The maximum HONO concentration was 7.59 ppb, which was observed during E1
238 (at 08:10 on December 8th). From December 11th to 12th the pollutants continuously increased with the
239 stagnant weather. The HONO concentrations remained at high levels, and the daytime mean HONO
240 mixing ratio even reached 3.1 ± 0.92 ppb. Figure 3 also shows the time series of simultaneously
241 measured other relevant species. The mean NO₂ mixing ratios during E1, C2, and E3 were 51.98 ± 8.41 ,
242 23.30 ± 11.91 , and 51.88 ± 5.97 ppb, respectively. Because NO and O₃ were not measured at ground
243 level after 14:00 on December 10th, the mean concentrations of NO and O₃ during E1 and C2 were
244 90.99 ± 67.98 and 14.66 ± 21.79 ppb, respectively, and 4.04 ± 1.81 and 14.37 ± 10.65 ppb, respectively.
245 After sunset, the concentration of O₃ at the surface was rapidly titrated due to the elevated NO and
246 increased with an increase in height. The mixing ratio of O₃ below 260 m was less than 9 ppb during
247 the vertical measurements. The BC, NR-PM₁, and aerosol surface area showed very similar patterns
248 both at ground level and at 260 m. The RH corrected aerosol surface area (S_{aw}) is shown in Fig. S2.
249 Higher BC, NR-PM₁ and S_{aw} levels were observed at ground level during the haze periods (E1 and E3).
250 Nocturnal stable surface layers of air generally form at low wind speeds ($< 6 \text{ m}\cdot\text{s}^{-1}$) (VandenBoer
251 et al., 2013). Hence, the vertical profile data were used when the wind speeds were less than $6 \text{ m}\cdot\text{s}^{-1}$,
252 except on December 7th. Vertical measurements during low wind events were successfully conducted
253 on three occasions (December 9–10, 10–11, and 11–12) and will be discussed below. The
254 near-continuous vertical measurements avoided the observation bias from prolonged fixed sampling.
255 The date and time of the measurement for each vertical profile is detailed in Table S1 in the
256 supplementary information.

257 **3.2 Nocturnal HONO vertical profiles**

258 **3.2.1 Vertical measurements after sunset**

259 Vertical measurements were conducted from ground level to 240 m after sunset. The mixing ratios
260 of HONO and NO₂ at ground level were consistent with those measured in the container. The mixing
261 ratios of HONO and NO₂ showed nearly flat profiles throughout the column during C2 and E3 (Fig.
262 S3), indicating that HONO and NO₂ were relatively well mixed after sunset. The vertical variations of
263 ΔHONO , which is the difference in the HONO concentrations between measured in the container and

264 at ground level, centered around 0 ppb and varied between -0.4 and 0.4 ppb. This result also indicated
265 the relatively uniform vertical distribution of HONO. The vertical variations in T and RH during these
266 three vertical measurements were similar (Fig. S4). While T decreased gradually with increasing
267 height, RH increased gradually with increasing height. In addition, RH was relatively higher during
268 the haze episode. Also, there was no T inversion just after sunset, and the consistent variations in the
269 HONO and NO_2 at ground level and in the vertical measurements all supported a relatively
270 well-mixed boundary layer, which explained the uniform vertical distribution of HONO and NO_2 .

271 3.2.2 Nocturnal vertical profiles

272 Nocturnal small-scale stratification and layering was determined according to the method of
273 Brown et al. (2012), who used the potential temperature profile as an indicator of atmospheric static
274 stability. According to the vertical variations in the potential temperature, the stable layer was divided
275 into the “surface layer”, the “nocturnal boundary layer (NBL)”, the “top of the nocturnal boundary
276 layer”, and the “residual layer (RL)”.

277 Figure 4 depicts the nocturnal vertical profiles of HONO, NO_2 , and potential temperature during
278 C2. The orthogonal linear least squares regression slope and correlation coefficients of HONO and NO_2
279 to altitude were applied to estimate the nocturnal gradient of HONO and NO_2 (Table 2). On the night of
280 December 9th (Fig. 4a), negative profiles of both HONO and NO_2 were clearly seen. When the
281 container ascended during 22:42–23:06, the potential temperature profile showed distinct stratification.
282 The surface layer extended to 10–20 m and the NBL extended to ~140 m. The obviously negative
283 gradient of HONO (-4.49 ± 0.31 ppt m^{-1}) and NO_2 (-14.38 ± 1.62 ppt m^{-1}) were observed throughout
284 the heights from 0 to 240 m. A negative gradient of HONO was observed in the RL, but was not
285 consistently observed in other measurements (see below). During the descent of the container from
286 23:15–23:40, the potential temperature profile showed that a shallow T inversion had rapidly formed
287 between 130 and 200 m. The obvious vertical variation in RH during 23:15–23:40 (Fig. S3) also
288 indicated the different layers at different heights, which was due to the influence of a shallow inversion
289 layer. Within the shallow inversion layer, vertical convection and transport were inhibited, and a
290 remarkable negative gradient was observed there. However, within the NBL, the negative gradient of
291 HONO and NO_2 disappeared. This might have been due to the continuous vertical mixing below the
292 shallow inversion layer from 23:06 to 23:40. Additionally, the surface source of HONO was obvious, as

293 evidenced by the apparently negative gradient of HONO in Table 2.

294 The vertical profile of potential temperature on December 10th (Fig. 4b) showed that a shallow
295 inversion layer formed between the surface layer and the NBL. In the shallow inversion layer, the
296 mixing ratios of HONO decreased rapidly with increasing height, and a significant negative gradient
297 was observed within the shallow inversion layer and surface layer. With the attenuation of the shallow
298 inversion layer during the descent of the container from 23:01 to 23:25, the inhibition of vertical
299 transport and mixing gradually weakened. The increase in the negative gradient of HONO and NO₂ and
300 the correlation coefficients of HONO and NO₂ to altitude from 22:36 to 23:25 also showed the
301 weakened shallow inversion layer near the surface, which suggested the nighttime HONO surface
302 source. The attenuation event of the shallow inversion layer may have also been the result of an
303 increase in the wind speed and the interaction of different air masses that changed from the west to
304 southeast between 15 and 100 m (Fig. S5). Above the 100 m height, the mixing ratio of HONO
305 decreased with increasing height, and the fluctuation in HONO was likely due to the interaction of
306 different air masses. In contrast, the vertical profiles of NO₂ showed that NO₂ rapidly decreased
307 towards the ground, and a significant positive gradient was observed near the surface that was caused
308 by several factors. Nocturnal NO₂ is produced by the reaction of O₃ with NO, which primarily occurs
309 near the surface, resulting in a negative gradient in NO₂. However, this effect was counteracted by the
310 dry deposition of NO₂, which by itself would result in a positive gradient (Stutz et al., 2004b).
311 Additionally, the mixing ratio of NO₂ was also affected by local traffic emission sources, and a
312 near-surface shallow inversion layer was formed on December 10th. All of these presumably led to a
313 clearly positive gradient for the near-surface NO₂. In contrast to the vertical profiles measured on
314 December 9th, a positive gradient observed in near-surface NO₂ on December 10th indicated that the
315 shallow inversion layer affected the vertical distribution of HONO and NO₂ at night.

316 Although the surface layer was a common feature in the potential temperature profiles, it was
317 absent during E3, and the NBL extended downward to the lowest measurement height (8 m above the
318 ground). As shown in Fig. 5, the vertical profile of HONO showed a significant negative gradient as the
319 container ascended during 22:35–23:00, and higher HONO mixing ratio was observed at ground level.
320 With the development of the boundary layer, the negative gradient of HONO continued to decrease
321 from 6.91 ± 0.33 ppt m⁻¹ during 22:35–23:00 to 1.79 ± 0.28 ppt m⁻¹ during 00:45–01:09 and even
322 disappeared between 00:00 and 00:26. Moreover, the consistent HONO/NO₂ ratios ($\sim 5.6\% \pm 0.3\%$)

323 were observed throughout the depth of the NBL between 23 and 01 h (Fig. S6). A near-steady state
324 plateau of the HONO mixing ratio and HONO/NO₂ was established near midnight with the NBL.
325 Similar vertical measurements were reported by VandenBoer et al (2013), who also observed a
326 near-steady state in the HONO mixing ratio and HONO/NO₂, and an approximate balance between the
327 production and loss of HONO late in the night. A possible physical and chemical process, the loss of
328 HONO to the ground surface due to dry deposition could account for the buildup and near-steady state
329 observed in the HONO mixing ratio and HONO/NO₂. This implied that significant quantities of HONO
330 were deposited to the ground surface at night.

331 The utility of the orthogonal linear least squares regression slope of HONO to altitude to estimate
332 the vertical gradient of HONO at night implies that the potential nocturnal HONO production from the
333 heterogeneous reaction of NO₂ on aerosol surface. A positive gradient of HONO (0.23 ± 0.36) between
334 00:00 and 00:26 was observed during E3. The aerosol surface area (S_{aw}) in the residual layer was
335 greater than $1500 \mu\text{m}^2 \text{cm}^{-3}$ throughout the night (range: $1592\text{-}2655 \mu\text{m}^2 \text{cm}^{-3}$). The S_{aw} was $2314 \mu\text{m}^2$
336 cm^{-3} from 22 to 01 h on December 11th and reached a maximum of $2569 \mu\text{m}^2 \text{cm}^{-3}$ in the residual layer.
337 These aerosol surface areas are a factor of 14-38 greater than that observed in previous studies of
338 HONO vertical gradient, which ranged between 60 and $158 \mu\text{m}^2 \text{cm}^{-3}$ (Kleffmann et al., 2003;
339 VandenBoer et al., 2013). Such high aerosol surface areas may provide a sufficient surface for the
340 heterogeneous reaction. The vertical profiles also showed an enhanced HONO/NO₂ ratios from C2 to
341 E3 (Fig. S7). Moreover, a relatively constant HONO mixing ratio and HONO/NO₂ ratio above 160 m
342 were observed from 22:35 to 01:09 during E3. Both of these observations are indicative of a potential
343 aerosol surface source of HONO aloft during the haze episode. Assuming that aerosol surface
344 production dominated the observed HONO mixing ratio in the overlying air during the haze episode,
345 the mixing ratios of HONO and NO₂ observed at 240 m and the aerosol surface area measured at 260 m
346 were parameterized to estimate the nocturnal production of HONO on aerosol surface, which is
347 explored in more detail in section 3.4.2.

348 **3.3 Direct emissions**

349 In the present study, the measurement site was surrounded by several main roads, and thus might
350 have been affected by vehicle emissions. CO and NO, as the primary pollutants, are emitted from
351 combustion processes like the burning of fossil fuels as well as vehicle emissions (Sun et al., 2014;

352 Tong et al., 2016; Bond et al., 2013). BC is another primary pollutant typically emitted from diesel
353 engines and residential solid fuels (Zhang et al., 2018). Good correlations of the nocturnal HONO with
354 CO ($R^2=0.85$), NO ($R^2=0.76$) and BC ($R^2=0.84$) at ground level were observed (Fig. S8), indicating the
355 potential effect of direct emissions on the observed HONO at night. The emission ratio of HONO/NO_x
356 have been determined from tunnel measurements in California (Kirchstetter et al., 1996), Germany
357 (Kurtenbach et al., 2001), and Hong Kong (Laing et al., 2017). However, considering the differences in
358 the type of vehicles, fuel compositions, and other factors, the reported emission factor of HONO/NO_x
359 might not be representative for the Beijing region. To evaluate the influence of direct emissions, the
360 local emission factor of HONO was derived from ambient measurements. Since NO was not measured
361 at ground level after December 10th, the nighttime measurement data of HONO and NO_x from
362 November 9th to December 10th were used to evaluate the local HONO emission factor.

363 Considering the potential secondary HONO formation with air mass aging during the transport
364 process, five criteria were applied to ensure as much of the freshly emitted air masses as possible: (a)
365 only nighttime data (from 18:00 LT to next 6:00 LT) were included to avoid the fast photolysis of
366 HONO; (b) only sharp peaks during nighttime and the elevations of HONO and NO_x over the
367 background levels were estimated; (c) $\Delta\text{NO}/\Delta\text{NO}_x > 0.80$; (d) good correlation between HONO and
368 NO_x; (e) short duration of the plume (< 30 min). The typical nighttime wind speed at measurement site
369 was 1.2 m s⁻¹, thus the duration for fresh air masses should have been less than 30 min during transport
370 from the emission to the measurement site. Criteria (b) and (c) were used as indicators for identifying
371 fresh vehicular emissions. Criteria (d) and (e) further confirmed that the increase in HONO was
372 primarily caused by freshly emitted plumes instead of heterogeneous reactions of NO₂.

373 Figure 6 shows two emission plumes observed on December 9th to 10th, 2016 based on the
374 preceding selection criteria. The slopes of HONO to NO_x can be considered as the emission ratios
375 (Rappenglück et al., 2013). The HONO/NO_x emission ratios were estimated for the 11 fresh emission
376 plumes that satisfied the preceding criteria (see Table 3). The derived emission factors of 0.78%–1.73%
377 had an average value of 1.28% ± 0.36%, which was larger than the 0.53%–0.8% measured in the tunnel
378 in Wuppertal (Kurtenbach et al., 2001). The minimum ratio of 0.78% approximated the value (0.8%)
379 measured in Wuppertal. It is worth mentioning that the value of 0.8% is widely used as the upper limit
380 of the HONO/NO_x emission ratio from road traffic in interpreting field observations and modeling
381 HONO emissions (Stutz et al., 2002; Su et al., 2008a; Tong et al., 2016). The maximum ratio of 1.73%

382 in this study is comparable to the value of 1.7% in Houston, Texas, observed by Rappenglück et al.
383 (2013). The derived emission ratios were within the range of other published results (0.19%–2.1%)
384 (Kirchstetter et al., 1996; Kurtenbach et al., 2001; Su et al., 2008a; Rappenglück et al., 2013; Yang et
385 al., 2014; Xu et al., 2015; Liang et al., 2017; Zhang et al., 2018; Li et al., 2018; Liu et al., 2019).
386 Comparisons of the derived HONO/NO_x ratios with the results obtained previously are summarized in
387 Table S2. To minimize the risk of overestimating the direct emissions, the minimum HONO/NO_x ratio
388 was used as an upper limit for the emission factor (Su et al., 2008a). The minimum HONO/NO_x ratio of
389 0.78% was used to evaluate the contribution of vehicle emissions to the ambient HONO levels at night
390 (Eq. (3)). In this case, the risk of overestimating direct emissions was minimized, but there was still the
391 effect of potential secondary HONO formation.

$$392 \quad [HONO]_{emis} = 0.0078 \times [NO_x] \quad (3)$$

393 where $[HONO]_{emis}$ and $[NO_x]$ are the HONO mixing ratios from vehicle emissions and the observed
394 NO_x mixing ratios, respectively. The direct emissions contributed an average of 29.3% ± 12.4% to the
395 ambient HONO concentrations at night, with an average HONO_{emis}/HONO value of 35.9% ± 11.8%
396 during the clean episode and an average HONO_{emis}/HONO value of 26% ± 11.3% during the haze
397 episode. The frequency distribution of HONO_{emis}/HONO during the clean and the haze episodes are
398 shown in Fig. 7. The lower vehicle emissions contribution during the haze episode could have been
399 caused by an odd-even car ban, which required alternate driving days for cars with even- and
400 odd-numbered license plates.

401 **3.4 Nocturnal HONO chemistry**

402 **3.4.1 Correlation studies**

403 The heterogeneous conversion of NO₂ is an important pathway for HONO formation during the
404 nighttime, as many field observations have found a good correlation between HONO and NO₂ (Zhou et
405 al., 2006; Su et al., 2008a; Wang et al., 2013; Huang et al., 2017). However, the use of a correlation
406 analysis to interpret the heterogeneous conversion of NO₂ should be treated carefully, as physical
407 transport and source emissions also contribute to the correlation. In this study, the correlations of
408 vertical profiles between HONO and NO₂ were analyzed. Vertical profile data without horizontal
409 transport were used to avoid the influence of physical transport. As shown in Fig. 8, the linear least
410 squares regression correlations of HONO to NO₂ exhibited moderate but significant correlations (C2:

411 $R^2 = 0.72$, E3: $R^2 = 0.69$), supporting that NO_2 participated in the formation of HONO. The column of
412 HONO and NO_2 showed a significantly positive correlation during the haze episode. However, the
413 negative correlation between HONO and NO_2 was observed at ground level during the haze episode
414 (Fig. S9), which was also observed in the previous ground-based observations (Hou et al., 2016; Zhang
415 et al., 2018). The observed significant correlation between the HONO column and NO_2 column could
416 be due to: (1) emissions and vertical mixing of HONO and NO_2 , and (2) a possible heterogeneous
417 reaction of NO_2 on aerosol surface.

418 Adsorbed water on a surface has been shown to affect the heterogeneous formation of HONO
419 (Stutz et al., 2004a). The relationship between HONO/ NO_2 and RH is illustrated in Fig. 9. Following
420 the method introduced by Stutz et al (2004a), the average of the five highest HONO/ NO_2 values in each
421 10% RH interval was evaluated to eliminate much of the influence of factors like the time of night,
422 advection, the surface density, etc. An increase in the HONO/ NO_2 ratio along with RH was observed at
423 each height interval when the RH was less than 70%. A previous observation at ground level also
424 reported that the HONO/ NO_2 ratio increased with an increase in RH when the RH was less than 70%. A
425 further increase in RH would lead to a decrease in the HONO/ NO_2 ratio, which was considered to be
426 caused by the number of water monolayers that formed on the surface leading to an efficient uptake of
427 HONO (Li et al., 2012; Yu et al., 2009; Liu et al., 2019). However, a decreased uptake coefficient of
428 HONO with increasing RH from 0% to 80% was observed in a laboratory study (Donaldson et al.,
429 2014). The NO_2 to HONO conversion efficiency depended negatively on RH at an RH above 70%,
430 which was presumably caused by the relative humidity affecting both HONO uptake onto the surface
431 and the NO_2 -to-HONO conversion. A decrease in the HONO/ NO_2 ratio with an increase in height at a
432 similar RH level were observed during C2 and E3. A higher conversion efficiency of NO_2 to HONO
433 was observed near the surface, and the HONO/ NO_2 ratios at different heights were significantly
434 different during C2. However, this differences decreased, and similar HONO/ NO_2 ratios were observed
435 at different heights during E3. This observation implied a possible heterogeneous conversion of NO_2 on
436 aerosol surface in the overlying air. It is necessary to note that the limited vertical measurements
437 resulted in a limited variation range in the RH, which limits this analysis. Additional efforts are needed
438 to conduct more comprehensive vertical measurements to interpret the HONO/ NO_2 ratios versus RH
439 for different heights in the future.

440 3.4.2 Relative importance of aerosol and ground surfaces in nocturnal HONO production

441 The observed positive HONO gradient implied a potential heterogeneous conversion of NO₂ on
 442 aerosol surface. The aerosol surface area observed during the haze episode was an order of magnitude
 443 higher than in other studies of HONO vertical gradient (Kleffmann et al., 2003; VandenBoer et al.,
 444 2013), which presumably provided sufficient aerosol surface area to account for the observed nighttime
 445 HONO production (Liu et al., 2019). The surface area information for particles larger than 0.5 μm were
 446 not valid at ground level and 260 m during the measurement periods. Hence, this is a lower limit
 447 estimate of the total surface area for the heterogeneous reaction.

448 An estimate of the nocturnal HONO production on aerosol surface was made using the RH
 449 corrected aerosol surface area (S_{aw}) and NO₂ observations from the residual layer. The CO and BC
 450 measured at ground level were independent of the CO and BC observed at 260 m during the haze
 451 period (Fig. S10), since it can be expected that air masses in the residual layer were decoupled from the
 452 ground-level processes and largely free of NO₂ emissions. (Brown et al., 2012; VandenBoer et al.,
 453 2013). The HONO production from the heterogeneous NO₂ conversion (Reaction R1) on aerosol
 454 surface would then have become the primary HONO source in the residual layer during E3. The yield
 455 of the hydrolysis reaction assumes that HONO and HNO₃ are formed by equimolar disproportionation
 456 of two NO₂ molecules and immediately release HONO (Finlayson-Pitts et al., 2003; Finlayson-Pitts,
 457 2009). The reactive uptake of NO₂ by the aerosols was assumed to occur on all measured aerosol
 458 surface areas, regardless of their chemical composition. HONO production ($P(HONO)$) can then be
 459 expressed using the equation of Ye et al. (2018) modified to account for the disproportionation:

$$460 \quad \frac{P(HONO)}{[NO_2]} = \frac{1}{8} \times S_{aw} \times \sqrt{\frac{8RT}{\pi M}} \times \gamma_{NO_2} \quad (4)$$

461 where γ_{NO_2} is the uptake coefficient, R is the gas constant, T is the absolute temperature (K), M is the
 462 molecular mass of NO₂ ($M=4.6 \times 10^{-2}$ kg mol⁻¹), and S_{aw} is the RH corrected aerosol surface area (μm²
 463 cm⁻³). The NO₂-normalized HONO production over time, $\Delta \frac{[HONO]}{[NO_2]}/\Delta t$, can be calculated using the
 464 following Eq. (5):

$$465 \quad \Delta \frac{[HONO]}{[NO_2]}/\Delta t \sim \frac{1}{8} \times S_{aw} \times \sqrt{\frac{8RT}{\pi M}} \times \gamma_{NO_2} \quad (5)$$

466 Assume an NO₂ uptake coefficient of 1×10^{-5} to 1×10^{-6} in the dark, which fits the NO₂ uptake
 467 coefficient values observed in relevant studies (J.Kleffmann et al., 1998; Kurtenbach et al., 2001;
 468 Saastad et al., 1993; Bröske et al., 2003). A representative temperature of 273 K, and an average observed

469 S_{av} of $2314 \mu\text{m}^2 \text{cm}^{-3}$ in the residual layer between 22 and 01 h during E3 were used. A relative HONO
470 accumulation rate of $\Delta \frac{[\text{HONO}]}{[\text{NO}_2]} / \Delta t$ ranged between 0.00037 and 0.0037h^{-1} , equivalent to the HONO
471 production of 0.02 to 0.2ppb h^{-1} at a constant NO_2 concentration of 54 ppb, which was the upper limit
472 of the observed nocturnal NO_2 in the residual layer during E3. The produced HONO amount of 30–300
473 ppt in an interval of 1.5 h could account for the HONO increases of 15–368 ppt in the residual layer
474 between the two vertical profile measurements. Thus, production from the heterogeneous conversion of
475 NO_2 solely on aerosol surface can explain the HONO observations during E3. In addition, if the HONO
476 production aloft was indeed dominated by reactions on aerosol surface, the column average
477 concentration of HONO would be expected to be independent of the amount of HONO observed at
478 ground level. Figure 10a shows that the column of HONO is independent of the mixing ratio of HONO
479 observed from the ground level to 10 m in height ($R^2 = 0.27$), which is consistent with the hypothesis
480 that the aerosol surface presumably dominates HONO production aloft by heterogeneous uptake of
481 NO_2 during the haze episode, and the production of HONO at ground level is not transported to the
482 overlying air. This result was contrary to previous observations that the production of HONO on
483 aerosol surface was insignificant compared to the ground surface (Kleffmann et al., 2003; Wong et al.,
484 2011; VandenBoer et al., 2013), which could have been due to the higher aerosol surface area observed
485 in this study. An order of magnitude higher aerosol surface area in the residual layer than in previous
486 vertical observations ($<160 \mu\text{m}^2 \text{cm}^{-3}$) was observed, which could provide sufficient aerosol surface
487 area for the heterogeneous formation of HONO.

488 An estimate of HONO production from the heterogeneous conversion of NO_2 on aerosols was also
489 made during C2 using S_{av} and NO_2 observations from the residual layer. The column of the average
490 HONO concentration was related to the amount of HONO observed between ground level and 10 m
491 (Fig. 10b, $R^2 = 0.93$), suggesting that the surface HONO sources affected the HONO observed
492 throughout the depth of boundary layer during C2. A high correlation ($R^2 = 0.83$) between the measured
493 CO and BC at ground level and the CO and BC at 260 m was also observed (Fig. S10), which indicated
494 that vehicle emissions affected air masses in the residual layer. The lack of the NO vertical profile
495 cannot directly correct the influence of direct HONO emissions. If it is assumed that the contribution of
496 direct HONO emissions was consistent at ground level and in the residual layer, the relative
497 contribution of the aerosol and ground surfaces to nocturnal HONO production in the residual layer

498 could be roughly estimated during C2. The direct emissions contribution of $35.9\% \pm 11.8\%$ during C2
499 is a higher limit estimate of the contribution of direct emissions to the HONO levels in the residual
500 layer.

501 The averages S_{av} of 791 and 894 $\mu\text{m}^2 \text{cm}^{-3}$ from 17 to 24 h, and an upper limit of NO_2
502 observations of 36 and 44 ppb from the residual layer were used to estimate HONO production on
503 aerosol surface on December 9th and 10th. The formation rates of HONO on aerosol surface were
504 0.0047–0.047 ppb h^{-1} on the 9th and 0.0062–0.062 ppb h^{-1} on the 10th. The HONO increased by 305–
505 608 ppt between profile measurements, which have the contributions from direct HONO emissions
506 subtracted, were higher than the production of HONO (26–259 ppt) in the interval of 5.5 h on
507 December 9th. The formation of HONO on aerosol surface cannot explain the observed HONO
508 increases in the residual layer, which suggests that the HONO observed in the residual layer was
509 primarily derived from the heterogeneous conversion of NO_2 on the ground surface followed by
510 vertical transport throughout the column. The HONO production from the aerosol surface in the
511 interval of 5.35 h was 33–332 ppt in the residual layer on December 10th, which was comparable to the
512 corrected HONO increases of 114–369 ppt between profile measurements. A shallow inversion layer
513 formed near the surface could account for the aerosols presumably dominated HONO production in the
514 residual layer, and this could have been due to the following: (1) the inhibition of vertical transport of
515 nighttime HONO source at ground level, and/or (2) an overestimation of the contribution from direct
516 HONO emissions to HONO concentrations in the residual layer.

517 In conclusion, HONO production solely on aerosol surface accounted for the HONO observations
518 during E3. The ground surface dominated HONO production by heterogeneous conversion of NO_2
519 during the clean episode, which was then transported throughout the column. With the increases in the
520 NO_2 mixing ratio and aerosol surface areas from the clean episode to the haze episode, the aerosol
521 surface production became an important nocturnal source of HONO and presumably dominated the
522 heterogeneous production of HONO aloft from NO_2 during the haze episode.

523 **3.4.3 Nocturnal HONO production and loss at ground level**

524 The nocturnal HONO observed throughout the depth of the boundary layer is primarily from the
525 heterogeneous conversion of NO_2 on the ground surface during the clean episode. The HONO
526 conversion frequency can be estimated using the data from the nocturnal measurements at ground level

527 (18:00–06:00 LT). The heterogeneous formation of HONO in reaction (R2) is first order in NO₂, and
 528 the HONO formation is proportional to the NO₂ concentration. The conversion frequency was derived
 529 using the method proposed by Alicke et al. (2002). The emission ratio of HONO/NO_x derived in
 530 section 3.3 was used to correct the HONO concentration by Eq. (6). Because NO was not measured at
 531 ground level after 14:00 on December 10th, the NO_x data was not available during the nocturnal vertical
 532 measurements on December 10th and 11th. The average HONO_{emis}/HONO ratio of 35.9% ± 11.8% and
 533 26% ± 11.3% were used to correct the observed HONO concentrations (i.e. [HONO]_{corr} =
 534 [HONO] – [HONO]_{emis}) during the clean and the haze episodes after December 10th, respectively. The
 535 NO₂-to-HONO conversion frequency, k_{HONO} , can be calculated using Eq. (7), by assuming that
 536 observed HONO comes from the conversion of NO₂ (Su et al., 2008a).

$$537 \quad [HONO]_{corr} = [HONO] - [NO_x] \times 0.0078 \quad (6)$$

$$538 \quad k_{HONO} = \frac{[HONO_{corr}]_{t_2} - [HONO_{corr}]_{t_1}}{(t_2 - t_1)[NO_2]} \quad (7)$$

539 where $\overline{[NO_2]}$ is the average NO₂ mixing ratio during the time interval of $t_2 - t_1$. The conversion
 540 frequencies, k_{HONO} , on December 9th, 10th, and 11th were 0.0082, 0.0060 and 0.0114 h⁻¹, respectively,
 541 corresponding to a HONO production rate by NO₂ (P_{NO_2}) of 0.25 ± 0.03, 0.28 ± 0.02, and 0.60 ± 0.02
 542 ppb h⁻¹ (i.e. $C_{HONO} \times \overline{[NO_2]}$), respectively. It is necessary to elaborate that the derived P_{NO_2} is the net
 543 HONO production, which means sources and sinks of HONO (aerosol and ground surface sources,
 544 deposition, etc.) have already been taken into account in the P_{NO_2} . The HONO conversion frequency
 545 obtained in this study is comparable to the observations by Hou et al. (2016) (clean episode: 0.0065 h⁻¹,
 546 haze episode: 0.0039 h⁻¹) and Zhang et al. (2018) in the Beijing region (haze episode: 0.058 h⁻¹, severe
 547 haze episode: 0.0146 h⁻¹). However, they are lower than the observations made by Li et al. (2012)
 548 (0.024 ± 0.015 h⁻¹) and Su et al. (2008b) (0.016 ± 0.014 h⁻¹) at a rural site in southern China.

549 It was assumed that production of HONO on aerosol surface was insignificant compared to the
 550 ground surface during the clean episode, which has been suggested in other studies of HONO vertical
 551 gradient (VandenBoer et al., 2013; Wong et al., 2011; Zhang et al., 2009). Therefore, the HONO
 552 production (P_{NO_2}) could be considered as a net contribution of the surface production of HONO to the
 553 total column of HONO when HONO deposition is considered in P_{NO_2} . The surface production rate of
 554 HONO of 0.25 ± 0.03 and 0.28 ± 0.02 ppb h⁻¹ were an order of magnitude higher than the maximum
 555 production rate of HONO on aerosol surface (0.047 and 0.062 ppb h⁻¹) on December 9th and 10th. This

556 result suggests that ground surface dominated HONO production by heterogeneous conversion of NO₂
 557 during the clean episode. In contrast, the production of HONO solely on aerosol surface can explain the
 558 HONO observations in the residual layer during E3, indicating that the aerosol surface production was
 559 an important nocturnal source of HONO during the haze episodes. The derived P_{NO_2} is the total
 560 HONO production rate of the aerosol and ground surfaces by heterogeneous conversion of NO₂. To
 561 compare the HONO heterogeneous production on aerosol and ground surfaces, a deposition velocity of
 562 NO₂ to the surface in the dark, V_{dep,NO_2} , of 0.07 cm s⁻¹ (VandenBoer et al., 2013), in a boundary layer
 563 of height, h of 140 m, was used to estimate the HONO production rate by NO₂ on the ground surface.
 564 The nocturnal production of HONO by heterogeneous uptake of NO₂ on ground surface can be
 565 estimated by the following,

$$566 \quad P_{HONO,ground} = \frac{1}{2} \frac{V_{dep,NO_2}}{h} \overline{[NO_2]} \quad (8)$$

567 The surface production rate of HONO ($P_{HONO,ground}$) was 0.47 ± 0.02 ppb h⁻¹ on December 11th (E3),
 568 which was comparable to the HONO production rate on aerosol surface of 0.2 ppb h⁻¹. This result also
 569 suggests that the production of HONO on aerosols is an important nocturnal source of HONO during
 570 the haze episode. The higher production rates of HONO on the ground surfaces were consistent with
 571 the fact that the ground had a much greater surface area than the aerosol (i.e., the ground surface area
 572 was 7140 μm² cm⁻³ in a 140 m deep NBL, versus the average S_{aw} of 2255 μm² cm⁻³ during E3).
 573 However, the vertical transport of the surface production of HONO throughout the column was likely
 574 inhibited during E3. The column average concentration of HONO was independent of the mixing ratio
 575 of HONO observed between ground level and 10 m (Fig. 10a), which may have been due to a more
 576 stable nocturnal boundary layer structure during the haze episode.

577 A budget equation of nighttime HONO (Eq. 9) was utilized to separate the contributions of the
 578 individual chemical processes involved in the nocturnal production and loss of HONO (Su et al., 2008b;
 579 Oswald et al., 2015).

$$580 \quad \frac{d[HONO]}{dt} = P_{emis} + P_{aerosol} + P_{ground} + P_A - L_{dep} \pm T_h \pm T_v \quad (9)$$

581 The production terms of the HONO consist of the direct emission rate (P_{emis}); the heterogeneous
 582 production rate on aerosol ($P_{aerosol}$) and ground surfaces (P_{ground}); and the additional nighttime
 583 HONO source/sink (P_A). The loss process (L_{dep}) is the dry deposition rate at nighttime. T_h and T_v
 584 describe the horizontal and vertical transport processes, respectively. The horizontal transport, T_h , is

585 negligible in a relative calm atmosphere with low wind speeds ($<1.6 \text{ m s}^{-1}$) during vertical
 586 measurements. The vertical transport, T_v , acts as a sink close to the surface and as an additional source
 587 at elevated levels. However, it is difficult to quantify T_v without direct measurements of fluxes or
 588 using the chemical transport model, and its contribution is uncertain. Without explicitly considering T_v ,
 589 the budget analysis is reasonable for relatively well-mixed conditions. Thus, the budget analysis is used
 590 for the measurements conducted on December 9th and 10th, when no shallow inversion layer was
 591 observed near the surface.

592 Simplifying Eq. (9), the $dHONO/dt$ was approximated by $\Delta HONO/\Delta t$, which is the difference
 593 in the observed HONO mixing ratios at two time points. An additional nocturnal production rate term
 594 (P_A) can be derived by Eq. (10). The emission ratio of HONO/ NO_x (0.78%) and HONO_{emis}/HONO ratio
 595 ($26\% \pm 11.3\%$) obtained in section 3.3 were used to estimate P_{emis} . The nocturnal production of
 596 HONO via NO_2 on aerosol and ground surfaces, and the production rate terms of $P_{aerosol}$ and
 597 P_{ground} in Eq. (4) and (8) were used as representations of the nocturnal production of HONO in Eq.
 598 (10). An upper limit uptake coefficient of γ_{NO_2} (1×10^{-5}) was assumed to estimate the HONO
 599 production rate on aerosol surface. For L_{dep} , the temperature-dependent deposition velocity of HONO
 600 ($V(HONO)_T = \exp(23920/T - 91.5)$) was used to estimate the $V_{dep,HONO}$, which decreased
 601 exponentially to non-significant values at 40 °C (Laufs et al., 2017). The average $V_{dep,HONO}$ calculated
 602 from the nocturnal measurements (00:00–06:00 LT) was 1.8 cm s^{-1} , with a range of values spanning 0.9
 603 to 3 cm s^{-1} , which was within the range of previously reported values between 0.077 and 3 cm s^{-1}
 604 (Harrison and Kitto, 1994; Harrison et al., 1996; Spindler et al., 1998; Stutz et al., 2002; Coe and
 605 Gallagher, 1992; Laufs et al., 2017).

$$606 \quad \frac{\Delta HONO}{\Delta t} = \frac{1}{2} \frac{V_{dep,NO_2}}{h} [NO_2] + \frac{1}{8} S_{aw} C_{NO_2} \gamma_{NO_2} [NO_2] + \frac{\Delta HONO_{emis}}{\Delta t} + P_A - \frac{V_{dep,HONO}}{h} [HONO] \quad (10)$$

607 Figure 11 shows the nocturnal HONO budgets from 18:00 to 06:00 LT on the 9th (C2) and 11th (E3)
 608 of December. The production rate of HONO on aerosol surface ($0.04 \pm 0.01 \text{ ppb h}^{-1}$) was insignificant
 609 compared to the ground surface ($0.28 \pm 0.03 \text{ ppb h}^{-1}$) during C2. However, an average $P_{aerosol}$ of 0.19
 610 $\pm 0.01 \text{ ppb h}^{-1}$ derived during E3 was comparable to the surface production rate of HONO (P_{ground} ,
 611 $0.47 \pm 0.03 \text{ ppb h}^{-1}$), which supported the preceding result that HONO production on aerosols was an
 612 important nocturnal source of HONO during the haze episode. For the source of direct HONO
 613 emissions, P_{emis} only provided a small portion of the HONO at a rate of 0.06 ± 0.07 and 0.10 ± 0.10

614 ppb h⁻¹. The loss of HONO due to surface deposition was the dominant sink for HONO during
615 nighttime. The L_{dep} contributed 0.74 ± 0.31 and 1.55 ± 0.32 ppb h⁻¹ to the nocturnal loss of HONO
616 during C2 and E3, respectively, implying that significant amounts of HONO were deposited to the
617 ground surface at night. This had been suggested in another study on the vertical gradient of HONO
618 (VandenBoer et al., 2013).

619 **4 Conclusions**

620 High-resolution vertical profiles of HONO and NO₂ were measured using an IBBCEAS
621 instrument during the APHH-Beijing winter campaign. To the best of our knowledge, this is the first
622 high-resolution vertical measurements of HONO and NO₂ in urban areas of China. The HONO
623 concentrations observed during E1, C2, and E3 were 4.26 ± 2.08 , 0.83 ± 0.65 , and 3.54 ± 0.91 ppb,
624 respectively. A relatively well-mixed boundary layer was observed after sunset, and the vertical
625 distribution of HONO was consistent with reduced mixing and stratification in the lower several
626 hundred meters of the nocturnal urban atmosphere. The small-scale stratification of the nocturnal
627 atmosphere and the formation of a shallow inversion layer affected the vertical distribution of HONO
628 and NO₂. A near-steady state in HONO mixing ratio and HONO/NO₂ ratio was observed near midnight
629 on December 11th to 12th, and an approximate balance was established between the production and loss
630 of HONO.

631 Direct HONO emissions contributed an average of $29.3\% \pm 12.4\%$ to the ambient HONO levels at
632 night. High-resolution vertical profiles of HONO revealed (1) the ground surface dominated HONO
633 production by heterogeneous conversion of NO₂ during the clean episode, (2) the production solely on
634 aerosols explained the HONO observations in the residual layer during E3, suggesting that the aerosols
635 was an important nighttime HONO source during the haze episode. The column average HONO
636 concentration was irrelevant to the HONO observed between the ground level and 10 m during E3,
637 implying that the aerosols presumably dominated the heterogeneous production of HONO aloft from
638 NO₂ during the haze episode. Average dry deposition rates of 0.74 ± 0.31 and 1.55 ± 0.32 ppb h⁻¹ were
639 identified during the clean and haze episodes, respectively, implying that significant amounts of HONO
640 were deposited to the ground surface at night. Overall, these results draw a picture of the nocturnal
641 sources of HONO during different pollution levels, and demonstrated the urgent need for
642 high-resolution vertical measurements of HONO to a high height (e.g., using tethered balloons) and

643 more comprehensive vertical observations to improve our understanding of the vertical distribution and
644 chemistry of HONO in the PBL.

645

646 *Data availability.* The data used in this study are available from the corresponding author upon request
647 (mqin@aiofm.ac.cn).

648

649 *Supplement.*

650

651 *Author contributions.* MQ and PX organized the field contributions from the Anhui Institute of Optics and Fine
652 Mechanics group for the APHH-Beijing project. MQ and JD designed the study. WF and JD built the IBBCEAS
653 instrument. JD and KT collected the HONO and NO₂ data. YS and CX provided the ancillary data. FM and MQ
654 analyzed the data. FM wrote the paper and MQ revised it. The contributions of FM and MQ are the same for this
655 paper.

656

657 *Competing interests.* The authors declare that they have no conflict of interest.

658

659 *Special issue statement.* This article is part of the special issue “In-depth study of air pollution sources and
660 processes within Beijing and its surrounding region (APHH-Beijing) (ACP/AMT inter-journal SI)”. It is not
661 associated with a conference.

662

663 *Acknowledgements.* We gratefully acknowledge Bin Ouyang from Cambridge University for providing HONO
664 measurement data for inter-comparison.

665

666 *Financial support.* This work was supported by the National Natural Science Foundation of China (41875154,
667 41571130023, 91544104), the National Key R&D Program of China (2017YFC0209400, 2016YFC0208204), and
668 the Science and Technology Major Special Project of Anhui Province, China (16030801120).

669

670

671

672 **References**

- 673 Aliche, B., Platt, U., Stutz, J.: Impact of nitrous acid photolysis on the total hydroxyl radical budget during the
674 Limitation of Oxidant Production/Pianura Padana Produzione di Ozono study in Milan, J. Geophys. Res., 107,
675 LOP 9-1-LOP 9-17, <https://doi.org/10.1029/2000jd000075>, 2002.
- 676 Ammann, M., Kalberer, M., Jost, D. T., Tobler, L., Rossler, E., Pignatelli, D., Gaggeler, H. W., and Baltensperger, U.:
677 Heterogeneous production of nitrous acid on soot in polluted air masses, Nature, 395, 157-160,
678 <https://doi.org/10.1038/25965>, 1998.
- 679 An, J., Li, Y., Chen, Y., Li, J., Qu, Y., and Tang, Y. J.: Enhancements of major aerosol components due to additional
680 HONO sources in the North China Plain and implications for visibility and haze, Adv. Atmos. Sci., 30, 57-66,
681 <https://doi.org/10.1007/s00376-012-2016-9>, 2012.
- 682 Aubin, D. G., and Abbatt, J. P. D.: Interaction of NO₂ with Hydrocarbon Soot: Focus on HONO Yield, Surface
683 Modification, and Mechanism, J. Phys. Chem. A., 111, 6263-6273, <https://doi.org/10.1021/jp068884h>, 2007.
- 684 Bao, F. X., Li, M., Zhang, Y., Chen, C. C., and Zhao, J. C.: Photochemical Aging of Beijing Urban PM_{2.5}: HONO
685 Production, Environ. Sci. Technol., 52, 6309-6316, <https://doi.org/10.1021/acs.est.8b00538>, 2018.
- 686 Bartolomei, V., Alvarez, E. G., Wittmer, J., Thili, S., Strekowski, R., Temime-Roussel, B., Quivet, E., Wortham, H.,
687 Zetzsch, C., Kleffmann, J., and Gligorovski, S.: Combustion Processes as a Source of High Levels of Indoor
688 Hydroxyl Radicals through the Photolysis of Nitrous Acid, Environ. Sci. Technol., 49, 6599-6607,
689 <https://doi.org/10.1021/acs.est.5b01905>, 2015.
- 690 Bejan, I., Abd-El-Aal, Y., Barnes, I., Benter, T., Bohn, B., Wiesen, P., and Kleffmann, J.: The photolysis of
691 *ortho*-nitrophenols: a new gas phase source of HONO, Phys. Chem. Chem. Phys., 8, 2028-2035,
692 <https://doi.org/10.1039/b516590c>, 2006.
- 693 Bond, T. C., Doherty, S. J., Fahey, D. W., Forster, P. M., Berntsen, T., DeAngelo, B. J., Flanner, M. G., Ghan, S.,
694 Kärcher, B., Koch, D., Kinne, S., Kondo, Y., Quinn, P.K., Sarofim, M.C., Schultz, M.G., Schulz, M., Venkataraman,
695 C., Zhang, H., Zhang, S., Bellouin, N., Guttikunda, S.K., Hopke, P.K., Jacobson, M.Z., Kaiser, J.W., Klimont, Z.,
696 Lohmann, U., Schwarz, J.P., Shindell, D., Storelvmo, T., Warren, S.G., and Zender, C.S.: Bounding the role of
697 black carbon in the climate system: A scientific assessment, J. Geophys. Res. Atmos., 118, 5380-5552,
698 <https://doi.org/10.1002/jgrd.50171>, 2013.
- 699 Brigante, M., Cazoir, D., D'Anna, B., George, C., and Donaldson, D. J.: Photoenhanced Uptake of NO₂ by Pyrene
700 Solid Films, J. Phys. Chem. A, 112, 9503-9508, <https://doi.org/10.1021/jp802324g>, 2008.
- 701 Bröske, R., Kleffmann, J., and Wiesen, P.: Heterogeneous conversion of NO₂ on secondary organic aerosol
702 surfaces: A possible source of nitrous acid (HONO) in the atmosphere?, Atmos. Chem. Phys., 3, 469-474,
703 <https://doi.org/10.5194/acp-3-469-2003>, 2003.
- 704 Brown, S. S., Dubé, W. P., Osthoff, H. D., Wolfe, D. E., Angevine, W. M., and Ravishankara, A. R.: High
705 resolution vertical distributions of NO₃ and N₂O₅ through the nocturnal boundary layer, Atmos. Chem. Phys., 7,
706 139-149, <https://doi.org/10.5194/acp-7-139-2007>, 2007.
- 707 Cai, R. L., Yang, D. S., Fu, Y. Y., Wang, X., Li, X. X., Ma, Y., Hao, J. M., Zheng, J., and Jiang, J. K.: Aerosol
708 surface area concentration: a governing factor in new particle formation in Beijing, Atmos. Chem. Phys., 17,
709 12327-12340, <https://doi.org/10.5194/acp-17-12327-2017>, 2017.
- 710 Coe, H., and Gallagher, M. W.: Measurements of Dry Deposition of NO₂ to A Dutch Heathland Using the
711 Eddy-Correlation Technique, Q. J. Roy. Meteor. Soc., 118, 767-786, <https://doi.org/10.1002/qj.49711850608>, 1992.
- 712 Cui, L. L., Li, R., Zhang, Y. C., Meng, Y., Fu, H. B. and Chen, J. M.: An observational study of nitrous acid
713 (HONO) in Shanghai, China: The aerosol impact on HONO formation during the haze episodes, Sci. Total
714 Environ., 630, 1057-1070, <https://doi.org/10.1016/j.scitotenv.2018.02.063>, 2018.
- 715 Donaldson, M. A., Berke, A. E., and Raff, J. D.: Uptake of Gas Phase Nitrous Acid onto Boundary Layer Soil

716 Surfaces, *Environ. Sci. Technol.*, 48, 375-383, <https://doi.org/10.1021/es404156a>, 2014.

717 Du, W., Zhao, J., Wang, Y. J., Zhang, Y. J., Wang, Q. Q., Xu, W. Q., Chen, C., Han, T. T., Zhang, F., Li, Z. Q., Fu, P.

718 Q., Li, J., Wang, Z. F., and Sun, Y. L.: Simultaneous measurements of particle number size distributions at ground

719 level and 260 m on a meteorological tower in urban Beijing, China, *Atmos. Chem. Phys.*, 17, 6797-6811,

720 <https://doi.org/10.5194/acp-17-6797-2017>, 2017.

721 Duan, J., Qin, M., Ouyang, B., Fang, W., Li, X., Lu, K. D., Tang, K., Liang, S. X., Meng, F. H., Hu, Z. K., Xie, P.

722 H., Liu, W. Q., and Häsler, R.: Development of an incoherent broadband cavity-enhanced absorption spectrometer

723 for in situ measurements of HONO and NO₂, *Atmos. Meas. Tech.*, 11, 4531-4543,

724 <https://doi.org/10.5194/amt-11-4531-2018>, 2018.

725 Finlayson-Pitts, B. J., Wingen, L. M., Sumner, A. L., Syomin, D., and Ramazan, K. A.: The heterogeneous

726 hydrolysis of NO₂ in laboratory systems and in outdoor and indoor atmospheres: An integrated mechanism, *Phys.*

727 *Chem. Chem. Phys.*, 5, 223-242, <https://doi.org/10.1039/b208564j>, 2003.

728 Finlayson-Pitts, B. J.: Reactions at surfaces in the atmosphere: integration of experiments and theory as necessary

729 (but not necessarily sufficient) for predicting the physical chemistry of aerosols, *Phys. Chem. Chem. Phys.*, 36,

730 7760-7779, <https://doi.org/10.1039/B906540G>, 2009.

731 George, C., Strekowski, R. S., Kleffmann, J., Stemmler, K., and Ammann, M.: Photoenhanced uptake of gaseous

732 NO₂ on solid organic compounds: a photochemical source of HONO?, *Faraday Discuss.*, 130, 195-210,

733 <https://doi.org/10.1039/b417888m>, 2005.

734 Gómez Alvarez, E., Sörgel, M., Gligorovski, S., Bassil, S., Bartolomei, V., Coulomb, B., Zetzsch, C., and Wortham,

735 H.: Light-induced nitrous acid (HONO) production from NO₂ heterogeneous reactions on household chemicals,

736 *Atmos. Environ.*, 95, 391-399, <https://doi.org/10.1016/j.atmosenv.2014.06.034>, 2014.

737 Han, C., Yang, W. J., Wu, Q. Q., Yang, H., and Xue, X. X.: Heterogeneous Photochemical Conversion of NO₂ to

738 HONO on the Humic Acid Surface under Simulated Sunlight, *Environ. Sci. Technol.*, 50, 5017-5023,

739 <https://doi.org/10.1021/acs.est.5b05101>, 2016.

740 Han, C., Yang, W. J., Yang, H., and Xue, X. X.: Enhanced photochemical conversion of NO₂ to HONO on humic

741 acids in the presence of benzophenone, *Environ. Pollut.*, 231, 979-986,

742 <https://doi.org/10.1016/j.envpol.2017.08.107>, 2017.

743 Hanst, P. L., Spence, J. W., and Miller, M.: Atmospheric Chemistry of N-nitroso Dimethylamine, *Environ. Sci.*

744 *Technol.*, 11, 403-405, <https://doi.org/10.1021/es60127a007>, 1977.

745 Harrison, R. M., and Kitto, A. M. N.: Evidence for a surface source of atmospheric nitrous acid, *Atmos. Environ.*,

746 28, 1089-1094, [https://doi.org/10.1016/1352-2310\(94\)90286-0](https://doi.org/10.1016/1352-2310(94)90286-0), 1994.

747 Harrison, R. M., Peak, J. D., and Collins, G. M.: Tropospheric cycle of nitrous acid, *J. Geophys. Res.*, 101,

748 14429-14439, <https://doi.org/10.1029/96JD00341>, 1996.

749 Hendrick, F., Müller, J. F., Clémer, K., Wang, P., De Mazière, M., Fayt, C., Gielen, C., Hermans, C., Ma, J. Z.,

750 Pinardi, G., Stavrou, T., Vlemmix, T., and Van Roozendaal, M.: Four years of ground-based MAX-DOAS

751 observations of HONO and NO₂ in the Beijing area, *Atmos. Chem. Phys.*, 14, 765-781,

752 <https://doi.org/10.5194/acp-14-765-2014>, 2014.

753 Hou, S. Q., Tong, S. R., Ge, M. F., and An, J. L.: Comparison of atmospheric nitrous acid during severe haze and

754 clean periods in Beijing, China, *Atmos. Environ.*, 124, 199-206, <https://doi.org/10.1016/j.atmosenv.2015.06.023>,

755 2016.

756 Huang, R. J., Yang, L., Cao, J. J., Wang, Q. Y., Tie, X. X., Ho, K. F., Shen, Z. X., Zhang, R. J., Li, G. H., Zhu, C. S.,

757 Zhang, N. N., Dai, W. T., Zhou, J. M., Liu, S. X., Chen, Y., Chen, J., and O'Dowd, C. D.: Concentration and

758 sources of atmospheric nitrous acid (HONO) at an urban site in Western China, *Sci. Total Environ.*, 593-594,

759 165-172, <https://doi.org/10.1016/j.scitotenv.2017.02.166>, 2017.

760 Hao, N., Zhou, B., Chen, D., and Chen, L. M.: Observations of nitrous acid and its relative humidity dependence
761 in Shanghai, *J. Environ. Sci.*, 18, 910-915, [https://doi.org/10.1016/S1001-0742\(06\)60013-2](https://doi.org/10.1016/S1001-0742(06)60013-2), 2006.

762 Karamchandani, P., Emery, C., Yarwood, G., Lefer, B., Stutz, J., Couzo, E., and Vizuete, W.: Implementation and
763 refinement of a surface model for heterogeneous HONO formation in a 3-D chemical transport model, *Atmos.*
764 *Environ.*, 112, 356-368, <https://doi.org/10.1016/j.atmosenv.2015.01.046>, 2015.

765 Kirchstetter, T. W., Harley, R. A., and Littlejohn D.: Measurement of nitrous acid in motor vehicle exhaust,
766 *Environ. Sci. Technol.*, 30, 2843-2849, <https://doi.org/10.1021/es960135y>, 1996.

767 Kleffmanna, J., Beckera, K. H., and Wiesena, P.: Heterogeneous NO₂ conversion processes on acid surfaces:
768 possible atmospheric implications, *Atmos. Environ.*, 32, 2721-2729,
769 [https://doi.org/10.1016/S1352-2310\(98\)00065-X](https://doi.org/10.1016/S1352-2310(98)00065-X), 1998.

770 Kleffmann, J., Becker, K. H., Lackhoff, M., and Wiesen, P.: Heterogeneous conversion of NO₂ on carbonaceous
771 surfaces, *Phys. Chem. Chem. Phys.*, 1, 5443-5450, <https://doi.org/10.1039/A905545B>, 1999.

772 Kleffmann, J., Kurtenbach, R., Lörzer, J., Wiesen, P., Kalthoff, N., Vogel, B., and Vogel, H.: Measured and
773 simulated vertical profiles of nitrous acid—Part I: Field measurements, *Atmos. Environ.*, 37, 2949-2955,
774 [https://doi.org/10.1016/s1352-2310\(03\)00242-5](https://doi.org/10.1016/s1352-2310(03)00242-5), 2003.

775 Kleffmann, J.: Daytime Sources of Nitrous acid (HONO) in the Atmospheric Boundary Layer, *Chemphyschem*, 8,
776 1137-1144, <https://doi.org/10.1002/cphc.200700016>, 2007.

777 Kurtenbach, R., Becker, K. H., Gomes, J. A. G., Kleffmann, J., Lörzer, J., Spittler, M., Wiesen, P., Ackermann, R.,
778 Geyer, A., and Platt, U.: Investigations of emission and heterogeneous formation of HONO in a road traffic tunnel,
779 *Atmos. Environ.*, 35, 3385–3394, [https://doi.org/10.1016/S1352-2310\(01\)00138-8](https://doi.org/10.1016/S1352-2310(01)00138-8), 2001.

780 Laufs, S., Cazaunau, M., Stella, P., Kurtenbach, R., Cellier, P., Mellouki, A., Loubet, B., and Kleffmann, J.: Diurnal
781 fluxes of HONO above a crop rotation, *Atmos. Chem. Phys.*, 17, 6907-6923,
782 <https://doi.org/10.5194/acp-17-6907-2017>, 2017.

783 Li, D. D., Xue, L. K., Wen, L., Wang, X. F., Chen, T. S., Mellouki, A., Chen, J. M., and Wang, W. X.:
784 Characteristics and sources of nitrous acid in an urban atmosphere of northern China: Results from 1-yr continuous
785 observations, *Atmos. Environ.*, 182, 296-306, <https://doi.org/10.1016/j.atmosenv.2018.03.033>, 2018.

786 Li, S. P., Matthews, J., and Sinha, A.: Atmospheric Hydroxyl Radical Production from Electronically Excited NO₂
787 and H₂O, *Science*, 319, 1657-1660, <https://doi.org/10.1126/science.1151443>, 2008.

788 Li, X., Brauers, T., Häsel, R., Bohn, B., Fuchs, H., Hofzumahaus, A., Holland, F., Lou, S., Lu, K. D., Rohrer, F.,
789 Hu, M., Zeng, L. M., Zhang, Y. H., Garland, R. M., Su, H., Nowak, A., Wiedensohler, A., Takegawa, N., Shao, M.,
790 and Wahner, A.: Exploring the atmospheric chemistry of nitrous acid (HONO) at a rural site in Southern China,
791 *Atmos. Chem. Phys.*, 12, 1497-1513, <https://doi.org/10.5194/acp-12-1497-2012>, 2012.

792 Li, X., Rohrer, F., Hofzumahaus, A., Brauers, T., Häsel, R., Bohn, B., Broch, S., Fuchs, H., Gomm, H., Holland,
793 F., Jäger, J., Kaiser, J., Keutsch, F. N., Lohse, I., Lu, K. D., Tillmann, R., Wegener, R., Wolfe, G. M., Mentel, T. F.,
794 Kiendler-Scharr, A., Wahner, A.: Missing Gas-Phase Source of HONO Inferred from Zeppelin Measurement in the
795 Troposphere, *Science*, 334, 292-296, <https://doi.org/10.1126/science.1248999>, 2014.

796 Liang, Y. T., Zha, Q. Z., Wang, W. H., Cui, L., Lui, K. H., Ho, K. F., Wang, Z., Lee, S. C., and Wang, T.: Revisiting
797 nitrous acid (HONO) emission from on-road vehicles: A tunnel study with a mixed fleet, *J. Air Waste Manag.*, 67,
798 797-805, <https://doi.org/10.1080/10962247.2017.1293573>, 2017.

799 Liu, X., Cheng, Y., Zhang, Y., Jung, J., Sugimoto, N., Chang, S.Y., Kim, Y. J., Fan, S., and Zeng, L.: Influences of
800 relative humidity and particle chemical composition on aerosol scattering properties during the 2006 PRD
801 campaign, *Atmos. Environ.*, 42, 1525–1536, <https://doi.org/10.1016/j.atmosenv.2007.10.077>, 2008.

802 Liu, Y. H., Lu, K. D., Li, X., Dong, H. B., Tan, Z. F., Wang, H. C., Zou, Q., Wu, Y. S., Zeng, L. M., Hu, M., Min, K.
803 E., Kecorius, S., Wiedensohler, A., and Zhang, Y. H.: A Comprehensive Model Test of the HONO Sources

804 Constrained to Field Measurements at Rural North China Plain, *Environ. Sci. Technol.*, 53, 3517-3525,
805 <https://doi.org/10.1021/acs.est.8b06367>, 2019.

806 Liu, Y. L., Nie, W., Xu, Z., Wang, T. Y., Wang, R. X., Li, Y. Y., Wang, L., Chi, X. G., and Ding, A. J.:
807 Semi-quantitative understanding of source contribution to nitrous acid (HONO) based on 1 year of continuous
808 observation at the SORPES station in eastern China, *Atmos. Chem. Phys.*, 19, 13289-13308,
809 <https://doi.org/10.5194/acp-19-13289-2019>, 2019.

810 Liu, Z., Wang, Y. h., Costabile, F., Amoroso, A., Zhao, C., Huey, L. G., Stickel, R., Liao, J., and Zhu, T.: Evidence
811 of Aerosols as a Media for Rapid Daytime HONO Production over China, *Environ. Sci. Technol.*, 48, 14386-14391,
812 <https://doi.org/10.1021/es504163z>, 2014.

813 Liu, Z., Wang, Y., Gu, D., Zhao, C., Huey, L. G., Stickel, R., Liao, J., Shao, M., Zhu, T., Zeng, L., Amoroso, A.,
814 Costabile, F., Chang, C.-C., and Liu, S.-C.: Summertime photochemistry during CAREBeijing-2007:RO_x budgets
815 and O₃ formation, *Atmos. Chem. Phys.*, 12, 7737-7752, <https://doi.org/10.5194/acp-12-7737-2012>, 2012.

816 Lu, K. D., Rohrer, F., Holland, F., Fuchs, H., Bohn, B., Brauers, T., Chang, C. C., Häsel, R., Hu, M., Kita, K.,
817 Kondo, Y., Li, X., Lou, S. R., Nehr, S., Shao, M., Zeng, L. M., Wahner, A., Zhang, Y. H., and Hofzumahaus, A.:
818 Observation and modelling of OH and HO₂ concentrations in the Pearl River Delta 2006: a missing OH source in a
819 VOC rich atmosphere, *Atmos. Chem. Phys.*, 12, 1541-1569, <https://doi.org/10.5194/acp-12-1541-2012>, 2012.

820 Ma, Q. X., Wang, T., Liu, C., He, H., Wang, Z., Wang, W. H., and Liang, Y. T.: SO₂ Initiates the Efficient
821 Conversion of NO₂ to HONO on MgO Surface, *Environ. Sci. Technol.*, 51, 3767-3775,
822 <https://doi.org/10.1021/acs.est.6b05724>, 2017.

823 Mendez, M., Blond, N., Amedro, D., Hauglustaine, D. A., Blondeau, P., Afif, C., Fittschen, C., and Schoemaeker,
824 C.: Assessment of indoor HONO formation mechanisms based on in situ measurements and modeling, *Indoor Air*,
825 27, 443-451, <https://doi.org/10.1111/ina.12320>, 2017.

826 Michoud, V., Colomb, A., Borbon, A., Miet, K., Beekmann, M., Camredon, M., Aumont, B., Perrier, S., Zapf, P.,
827 Siour, G., Ait-Helal, W., Afif, C., Kukui, A., Furger, M., Dupont, J. C., Haeffelin, M., and Doussin, J. F.: Study of
828 the unknown HONO daytime source at a European suburban site during the MEGAPOLI summer and winter field
829 campaigns, *Atmos. Chem. Phys.*, 14, 2805-2822, <https://doi.org/10.5194/acp-14-2805-2014>, 2014.

830 Michoud, V., Doussin, J.-F., Colomb, A., Afif, C., Borbon, A., Camredon, M., Aumont, B., Legrand, M., and
831 Beekmann, M.: Strong HONO formation in a suburban site during snowy days, *Atmos. Environ.*, 116, 155-158,
832 <https://doi.org/10.1016/j.atmosenv.2015.06.040>, 2015.

833 Monge, M. E., D'Anna, B., Mazri, L., Giroir-Fendler, A., Ammann, M., Donaldson, D. J., and George, C.: Light
834 changes the atmospheric reactivity of soot, *P. Natl. Acad. Sci. USA*, 107, 6605-6609,
835 <https://doi.org/10.1073/pnas.0908341107>, 2010.

836 Oswald, R., Behrendt, T., Ermel, M., Wu, D., Su, H., Cheng, Y., Breuninger, C., Moravek, A., Mougins, E., Delon,
837 C., Loubet, B., Pommerening-Röser, A., Sörgel, M., Pöschl, U., Hoffmann, T., Andreae, M. O., Meixner, F. X. and
838 Trebs, I.: HONO Emissions from Soil Bacteria as a Major source of Atmospheric Reactive Nitrogen, *Science*, 341,
839 1233-1235, <https://doi.org/10.1126/science.1242266>, 2013.

840 Oswald, R., Ermel, M., Hens, K., Novelli, A., Ouwersloot, H. G., Paasonen, P., Petäjä, T., Sipilä, M., Keronen, P.,
841 Bäck, J., Königstedt, R., Hosaynali Beygi, Z., Fischer, H., Bohn, B., Kubistin, D., Harder, H., Martinez, M.,
842 Williams, J., Hoffmann, T., Trebs, I., and Sörgel, M.: A comparison of HONO budgets for two measurement
843 heights at a field station within the boreal forest in Finland, *Atmos. Chem. Phys.*, 15, 799-813,
844 <https://doi.org/10.5194/acp-15-799-2015>, 2015.

845 Pitts, J. N., Grosjean, D., Cauwenberghe, K. V., Schmid, J. P., and Fitz, D. R.: Photooxidation of aliphatic amines
846 under simulated atmospheric conditions: formation of nitrosamines, nitramines, amides, and photochemical
847 oxidant, *Environ. Sci. Technol.*, 12, 946-953, <https://doi.org/10.1021/es60144a009>, 1978.

848 Rappenglück, B., Lubertino, G., Alvarez, S., Golovko, J., Czader, B., and Ackermann, L.: Radical precursors and
849 related species from traffic as observed and modeled at an urban highway junction, *J. Air Waste Manag. Assoc.*, 63,
850 1270-1286, <https://doi.org/10.1080/10962247.2013.822438>, 2013.

851 Reisinger, A. R.: Observations of HNO₂ in the polluted winter atmosphere: possible heterogeneous production on
852 aerosols, *Atmos. Environ.*, 34, 3865-3874, [https://doi.org/10.1016/S1352-2310\(00\)00179-5](https://doi.org/10.1016/S1352-2310(00)00179-5), 2000.

853 Saastad, O. W., Ellermann, T., and Nielsen, C., J.: On the adsorption of NO and NO₂ on cold H₂O/H₂SO₄ surfaces,
854 *Geophys. Res. Lett.*, 20, 1191-1193, <https://doi.org/10.1029/93GL01621>, 1993.

855 Scharko, N. K., Martin, E. T., Losovj, Y., Peters, D. G., and Raff, J. D.: Evidence for Quinone Redox Chemistry
856 Mediating Daytime and Nighttime NO₂-to-HONO Conversion on Soil Surfaces, *Environ. Sci. Technol.*, 51,
857 9633-9643, <https://doi.org/10.1021/acs.est.7b01363>, 2017.

858 Sleiman, M., Gundel, L. A., Pankow, J. F., Jacob III, P., Singer, B. C., and Destailhats, H.: Formation of
859 carcinogens indoors by surface-mediated reactions of nicotine with nitrous acid, leading to potential thirdhand
860 smoke hazards, *P. Natl. Acad. Sci. USA*, 107, 6576-6581, <https://doi.org/10.1073/pnas.0912820107>, 2010.

861 Sörgel, M., Regelin, E., Bozem, H., Diesch, J. M., Drewnick, F., Fischer, H., Harder, H., Held, A.,
862 Hosaynali-Beygi, Z., Martinez, M., and Zetzsch, C.: Quantification of the unknown HONO daytime source and its
863 relation to NO₂, *Atmos. Chem. Phys.*, 11, 10433-10447, <https://doi.org/10.5194/acp-11-10433-2011>, 2011.

864 Spataro, F., Ianniello, A., Esposito, G., Allegrini, I., Zhu, T., and Hu, M.: Occurrence of atmospheric nitrous acid in
865 the urban area of Beijing (China), *Sci. Total Environ.*, 447, 210-224,
866 <https://doi.org/10.1016/j.scitotenv.2012.12.065>, 2013.

867 Spindler, G., Brüggemann, E., and Herrmann, H.: Nitrous acid (HNO₂) Concentration Measurements and
868 Estimation of Dry Deposition over Grassland in Eastern Germany, *Transactions on Ecology and Environment*, 28,
869 223-227, 1999.

870 Stemmler, K., Ammann, M., Donders, C., Kleffmann, J., and George, C.: Photosensitized reduction of nitrogen
871 dioxide on humic acid as a source of nitrous acid, *Nature*, 440, 195-198, <https://doi.org/10.1038/nature04603>,
872 2006.

873 Stutz, J., Alicke, B., Neftel, A.: Nitrous acid formation in the urban atmosphere: Gradient measurements of NO₂
874 and HONO over grass in Milan, Italy, *J. Geophys. Res.*, 107, LOP 5-1-LOP 5-15,
875 <https://doi.org/10.1029/2001JD000390>, 2002.

876 Stutz, J., Alicke, B., Ackermann, R., Geyer, A., Wang, S. H., White, A. B., Williams, E. J., Spicer, C. W., and Fast,
877 J. D.: Relative humidity dependence of HONO chemistry in urban areas, *J. Geophys. Res.-Atmos.*, 109, D03307,
878 <https://doi.org/10.1029/2003JD004135>, 2004a.

879 Stutz, J., Alicke, B., Ackermann, R., Geyer, A., White, A., and Williams, E.: Vertical profiles of NO₃, N₂O₅, O₃,
880 and NO_x in the nocturnal boundary layer: 1. Observations during the Texas Air Quality Study 2000, *J. Geophys. Res.-Atmos.*, 109, D12306, <https://doi.org/10.1029/2003JD004209>, 2004b.

882 Su, H., Cheng, Y. F., Cheng, P., Zhang, Y. H., Dong, S. F., Zeng, L. M., Wang, X. S., Slanina, J., Shao, M., and
883 Wiedensohler, A.: Observation of nighttime nitrous acid (HONO) formation at a non-urban site during
884 PRIDE-PRD2004 in China, *Atmos. Environ.*, 42, 6219-6232, <https://doi.org/10.1016/j.atmosenv.2008.04.006>,
885 2008a.

886 Su, H., Cheng, Y. F., Shao, M., Gao, D. F., Yu, Z. Y., Zeng, L. M., Slanina, J., Zhang, Y. H., and Wiedensohler, A.:
887 Nitrous acid (HONO) and its daytime sources at a rural site during the 2004 PRIDE-PRD experiment in China, *J.*
888 *Geophys. Res.*, 113, D14312, <https://doi.org/10.1029/2007JD009060>, 2008b.

889 Su, H., Cheng, Y. F., Oswald, R., Behrendt, T., Trebs, I., Meixner, F. X., Andreae, M. O., Cheng, P., Zhang, Y. H.,
890 and Pöschl, U.: Soil nitrite as a Source of Atmospheric HONO and OH Radicals, *Science*, 333, 1616-1618,
891 <https://doi.org/10.1126/science.1207687>, 2011.

892 Sun, Y. L., Wang, Z. F., Fu, P. Q., Yang, T., Jiang, Q., Dong, H. B., Li, J., and Jia, J. J.: Aerosol composition,
893 sources and processes during wintertime in Beijing, China, *Atmos. Chem. Phys.*, 13, 4577-4592,
894 <https://doi.org/10.5194/acp-13-4577-2013>, 2013.

895 Sun, Y. L., Jiang, Q., Wang, Z. F., Fu, P. Q., Li, J., Yang, T., and Yin, Y.: Investigation of the sources and evolution
896 processes of severe haze pollution in Beijing in January 2013, *J. Geophys. Res. Atmos.*, 119, 4380-4398,
897 <https://doi.org/10.1002/2014JD021641>, 2014.

898 Tan, Z. F., Fuchs, H., Lu, K. D., Hofzumahaus, A., Bohn, B., Broch, S., Dong, H. B., Gomm, S., Häsel, R., He, L.,
899 Y., Holland, F., Li, X., Liu, Y., Lu, S. H., Rohrer, F., Shao, M., Wang, B. L., Wang, M., Wu, Y. S., Zeng, L. M.,
900 Zhang, Y. S., Wahner, A., and Zhang, Y. H.: Radical chemistry at a rural site (Wangdu) in the North China Plain:
901 observation and model calculations of OH, HO₂ and RO₂ radicals, *Atmos. Chem. Phys.*, 17, 663-690,
902 <https://doi.org/10.5194/acp-17-663-2017>, 2017.

903 Tang, K., Qin, M., Duan, J., Fang, W., Meng, F. H., Liang, S. X., Xie, P. H., Liu, J. G., Liu, W. Q., Xue, C. Y., and
904 Mu, Y. J.: A dual dynamic chamber system based on IBBCEAS for measuring fluxes of nitrous acid in agricultural
905 fields in the North China Plain, *Atmos. Environ.*, 196, 10-19, <https://doi.org/10.1016/j.atmosenv.2018.09.059>,
906 2019.

907 Tang, Y., An, J., Wang, F., Li, Y., Qu, Y., Chen, Y., and Lin, J.: Impacts of an unknown daytime HONO source on
908 the mixing ratio and budget of HONO, and hydroxyl, hydroperoxyl, and organic peroxy radicals, in the coastal
909 regions of China, *Atmos. Chem. Phys.*, 15, 9381-9398, <https://doi.org/10.5194/acp-15-9381-2015>, 2015.

910 Tong, S. R., Hou, S. Q., Zhang, Y., Chu, B. W., Liu, Y. C., He, H., Zhao, P. S., and Ge, M. F.: Exploring the nitrous
911 acid (HONO) formation mechanism in winter Beijing: direct emissions and heterogeneous production in urban and
912 suburban areas, *Faraday Discuss.*, 189, 213-230, <https://doi.org/10.1039/c5fd00163c>, 2016.

913 Trinh, H. T., Imanishi, K., Morikawa, T., Hagino, H., and Takenaka N.: Gaseous nitrous acid (HONO) and nitrogen
914 oxides (NO_x) emission from gasoline and diesel vehicles under real-world driving test cycles, *J. Air Waste Manage.*
915 *Assoc.*, 67, 412-420, <https://doi.org/10.1080/10962247.2016.1240726>, 2017.

916 VandenBoer, T. C., Brown, S. S., Murphy, J. G., Keene, W. C., Young, C. J., Pszenny, A. A. P., Kim, S., Warneke,
917 C., de Gouw, J. A., Maben, J. R., Wagner, N. L., Riedel, T. P., Thornton, J. A., Wolfe, D. E., Dubé, W. P., Öztürk, F.,
918 Brock, C. A., Grossberg, N., Lefer, B., Lerner, B., Middlebrook, A. M., and Roberts, J. M.: Understanding the role
919 of the ground surface in HONO vertical structure: High resolution vertical profiles during NACHTT-11, *J. Geophys.*
920 *Res.- Atmos.*, 118, 10155-110171, <https://doi.org/10.1002/jgrd.50721>, 2013.

921 Villena, G., Kleffmann, J., Kurtenbach, R., Wiesen, P., Lissi, E., Rubio, M. A., Croxatto, G., and Rappenglück, B.:
922 Vertical gradients of HONO, NO_x and O₃ in Santiago de Chile, *Atmos. Environ.*, 45, 3867-3873,
923 <https://doi.org/10.1016/j.atmosenv.2011.01.073>, 2011.

924 Vogel, B., Vogel H., Kleffmann, J., and Kurtenbach, R.: Measured and simulated vertical profiles of nitrous
925 acid—Part II. Model simulations and indications for a photolytic source, *Atmos. Environ.*, 37, 2957-2966,
926 [https://doi.org/10.1016/S1352-2310\(03\)00243-7](https://doi.org/10.1016/S1352-2310(03)00243-7), 2003.

927 Wang, H. C., Lu, K. D., Chen, X. R., Zhu, Q. D., Wu, Z. J., Wu, Y. S., and Sun, K.: Fast particulate nitrate
928 formation via N₂O₅ uptake aloft in winter in Beijing, *Atmos. Chem. Phys.*, 18, 10483-10495,
929 <https://doi.org/10.5194/acp-18-10483-2018>, 2018.

930 Wang, J. Q., Zhang, X. S., Guo, J., Wang, Z. W., and Zhang, M. G.: Observation of nitrous acid (HONO) in Beijing,
931 China: Seasonal variation, nocturnal formation and daytime budget, *Sci. Total Environ.*, 587-588, 350-359,
932 <https://doi.org/10.1016/j.scitotenv.2017.02.159>, 2017.

933 Wang, S. S., Zhou, R., Zhao, H., Wang, Z. R., Chen, L. M., and Zhou, B.: Long-term observation of atmospheric
934 nitrous acid (HONO) and its implication to local NO₂ levels in Shanghai, China, *Atmos. Environ.*, 77, 718-724,
935 <https://doi.org/10.1016/j.atmosenv.2013.05.071>, 2013.

936 Wong, K. W., Oh, H. -J., Lefer, B. L., Rappenglück, B., and Stutz, J.: Vertical profiles of nitrous acid in the
937 nocturnal urban atmosphere of Houston, TX, *Atmos. Chem. Phys.*, 11, 3595-3609,
938 <https://doi.org/10.5194/acp-11-3595-2011>, 2011.

939 Wong, K. W., Tsai, C., Lefer, B., Haman, C., Grossberg, N., Brune, W. H., Ren, X., Luke, W., and Stutz, J.:
940 Daytime HONO vertical gradients during SHARP 2009 in Houston, TX, *Atmos. Chem. Phys.*, 12, 635-652,
941 <https://doi.org/10.5194/acp-12-635-2012>, 2012.

942 Wong, K. W., Tsai, C., Lefer, B., Grossberg, N., and Stutz, J.: Modeling of daytime HONO vertical gradients
943 during SHARP 2009, *Atmos. Chem. Phys.*, 13, 3587-3601, <https://doi.org/10.5194/acp-13-3587-2013>, 2013.

944 Xie, C. H., Xu, W. Q., Wang, J. F., Wang, Q. Q., Liu, D. T., Tang, G. Q., Chen, P., Du, W., Zhao, J., Zhang, Y. J.,
945 Zhou, W., Han, T. T., Bian, Q. Y., Li, J., Fu, P. Q., Wang, Z. F., Ge, X. L., Allan, J., Coe, H., and Sun, Y. L.: Vertical
946 characterization of aerosol optical properties and brown carbon in winter in urban Beijing, China, *Atmos. Chem.*
947 *Phys.*, 19, 165–179, <https://doi.org/10.5194/acp-19-165-2019>, 2019.

948 Xu, W. Q., Sun, Y. L., Wang, Q. Q., Zhao, J., Wang, J. F., Ge, X. L., Xie, C. H., Zhou, W., Du, W., Li, J., Fu, P. Q.,
949 Wang, Z. F., Worsnop, D. R., and Coe, H.: Changes in Aerosol Chemistry From 2014 to 2016 in Winter in Beijing:
950 Insights From High-Resolution Aerosol Mass Spectrometry, *J. Geophys. Res.- Atmos.*, 124, 1132-1147,
951 <https://doi.org/10.1029/2018JD029245>, 2019.

952 Xu, Z., Wang, T., Wu, J. Q., Xue, L. K., Chan, J., Zha, Q., Z., Zhou, S. Z., Louie, P. K. K., and Luk, C. W. Y.:
953 Nitrous acid (HONO) in a polluted subtropical atmosphere: Seasonal variability, direct vehicle emissions and
954 heterogeneous production at ground surface, *Atmos. Environ.*, 106, 100-109,
955 <https://doi.org/10.1016/j.atmosenv.2015.01.061>, 2015.

956 Yang, Q., Su, H., Li, X., Cheng, Y. F., Lu, K. D., Cheng, P., Gu, J. W., Guo, S., Hu, M., Zeng, L. M., Zhu, T., and
957 Zhang, Y. H.: Daytime HONO formation in the suburban area of the megacity Beijing, China, *Sci. China Chem.*,
958 57, 1032-1042, <https://doi.org/10.1007/s11426-013-5044-0>, 2014.

959 Ye, C. X., Zhang, N., Gao, H. L., and Zhou, X. L.: Photolysis of Particulate Nitrate as a Source of HONO and NO_x,
960 *Environ. Sci. Technol.*, 51, 6849-6856, <https://doi.org/10.1021/acs.est.7b00387>, 2017.

961 Ye, C. X., Zhou, X. L., Pu, D., Stutz, J., Festa, J., Spolaor, M., Tsai, C., Cantrell, C., Mauldin III, R. L.,
962 Weinheimer, A., Hornbrook, R. S., Apel, E. C., Guenther, A., Kaser, L., Yuan, B., Karl, T., Haggerty, J., Hall, S.,
963 Ullmann, K., Smith, J., and Ortega, J.: Tropospheric HONO distribution and chemistry in the southeastern US,
964 *Atmos. Chem. Phys.*, 18, 9107-9120, <https://doi.org/10.5194/acp-18-9107-2018>, 2018.

965 Yu, Y., Galle, B., Panday, A., Hodson, E., Prinn, R., and Wang, S.: Observations of high rates of NO₂-HONO
966 conversion in the nocturnal atmospheric boundary layer in Kathmandu, Nepal, *Atmos. Chem. Phys.*, 9, 6401-6415,
967 <https://doi.org/10.5194/acp-9-6401-2009>, 2009.

968 Zhang, N., Zhou, X. L., Shepson, P. B., Gao, H. L., Alaghmand, M., and Stirm, B.: Aircraft measurement of
969 HONO vertical profiles over a forested region, *Geophys. Res. Lett.*, 36, L15820,
970 <https://doi.org/10.1029/2009GL038999>, 2009.

971 Zhang, R., Wang, G., Guo, S., Zamora, M. L., Ying, Q., Lin, Y., Wang, W., Hu, M., and Wang, Y.: Formation of
972 Urban Fine Particulate Matter, *Chem. Rev.*, 115, 3303-3855, <https://doi.org/10.1021/acs/chemrev.5b00067>, 2015.

973 Zhang, W. Q., Tong, S. R., Ge, M. F., An, J. L., Shi, Z. B., Hou, S. Q., Xia, K. H., Qu, Y., Zhang, H. X., Chu, B. W.,
974 Sun, Y. L., and He, H.: Variations and sources of nitrous acid (HONO) during a severe pollution episode in Beijing
975 in winter 2016, *Sci. Total Environ.*, 648, 253-262, <https://doi.org/10.1016/j.scitotenv.2018.08.133>, 2018.

Table**Table 1.** Classification of the meteorological conditions and corresponding concentrations of NR-PM₁, NO₂ and HONO from December 7th to 12th.

Time period	Weather condition	NR-PM ₁ (μg·m ⁻³)	HONO (ppb)	NO ₂ (ppb)	WS (m·s ⁻¹)	WD	T (°C)	RH (%)
7 Dec–8 Dec (10:00)	Haze (E1)	30–184	1.49–7.59	24.91–65.48	0.03–1.95	NW-ESE ^a	1.6–9.3	36–82
8 Dec (10:00)–11 Dec	Clean (C2)	3–97	0.05–3.75	3.33–47.84	0.01–6.24	NE-NW	-2.4–9.1	16–53
11 Dec–12 Dec	Haze (E3)	69–217	1.54–5.51	38.58–66.57	0.02–1.81	NE-NW	-1.6–6.9	40–69

^a NE: Northeast; ESE: East-southeast; NW: Northwest;**Table 2.** The nocturnal gradient of HONO and NO₂ throughout the vertical measurements. The linear least squares regression slope and correlation coefficient of HONO and NO₂ to altitude identified in each vertical profile measurement.

Date	Time period (hh:mm, LT)	Gradient-HONO (ppt m ⁻¹)	R ²	Gradient-NO ₂ (ppt m ⁻¹)	R ²
9/12/2016	22:42–23:06	-4.49 ± 0.31	0.90	-14.38 ± 1.62	0.77
9/12/2016	23:15–23:40	-4.35 ± 0.70	0.62	-16.54 ± 1.85	0.77
10/12/2016	22:36–23:01	-1.08 ± 0.49	0.15	-2.97 ± 1.53	0.11
10/12/2016	23:01–23:25	-3.61 ± 0.50	0.60	-7.59 ± 1.24	0.62
11/12/2016	22:35–23:00	-6.91 ± 0.33	0.95	-9.53 ± 1.01	0.79
11/12/2016	23:04–23:29	-0.03 ± 0.43	0.0003	-5.32 ± 0.80	0.67
12/12/2016	00:00–00:26	0.23 ± 0.36	0.02	-5.21 ± 0.79	0.65
12/12/2016	00:45–01:09	-1.79 ± 0.28	0.64	-5.28 ± 0.84	0.63

Table 3. Emission ratios ($\Delta\text{HONO}/\Delta\text{NO}_x$) of the fresh direct emission plumes.

Date	Local Time	R ²	$\Delta\text{NO}/\Delta\text{NO}_x$	$\Delta\text{HONO}/\Delta\text{NO}_x$ (%)
15/11/2016	18:05–18:15	0.97	0.99	1.07
16/11/2016	20:50–21:10	0.83	0.96	0.92
24/11/2016	20:50–21:10	0.92	1.13	1.12
26/11/2019	02:10–02:40	0.94	0.94	1.31
26/11/2016	22:15–22:30	0.95	1.00	1.73
28/11/2019	04:40–04:55	0.87	0.85	0.78
29/11/2016	03:30–03:50	0.95	0.98	1.60
2/12/2016	23:40–23:55	0.95	1.01	1.67
7/12/2016	02:25–02:35	0.87	0.90	1.67
10/12/2016	01:00–01:25	0.84	0.95	1.43
10/12/2016	02:40–02:55	0.86	0.93	0.79

Figures

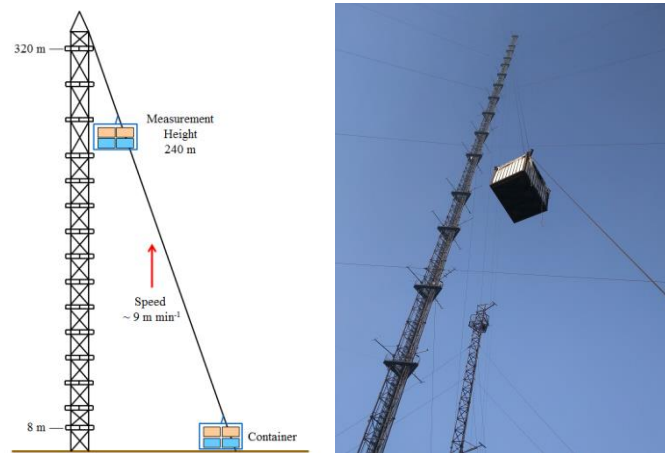


Figure 1. The Beijing 325-m meteorological tower (BMT) at the Institute of Atmospheric Physics (IAP).

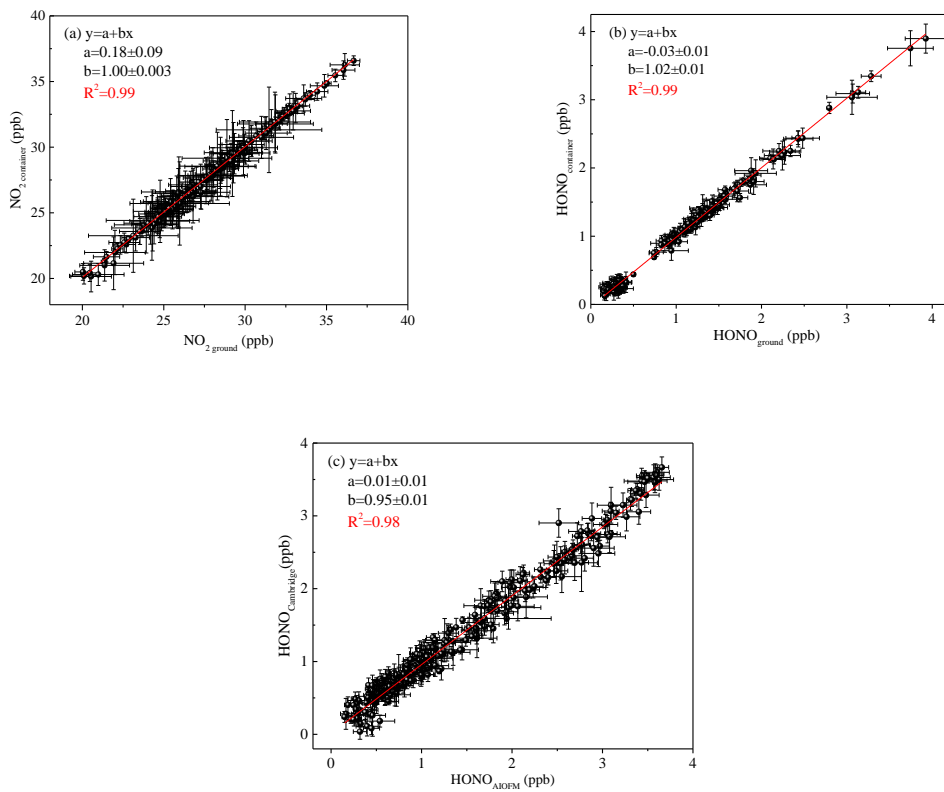


Figure 2. (a) Correlation of NO_2 concentration was measured using the two IBBCEAS instruments; (b) correlation of HONO concentration was measured using the two IBBCEAS instruments; (c) an inter-comparison between the IBBCEAS of Cambridge University and the IBBCEAS of the Anhui Institute of Optics and Fine Mechanics (AIOFM). The solid lines (red lines) show the orthogonal linear least squares regression between the two IBBCEAS instruments.

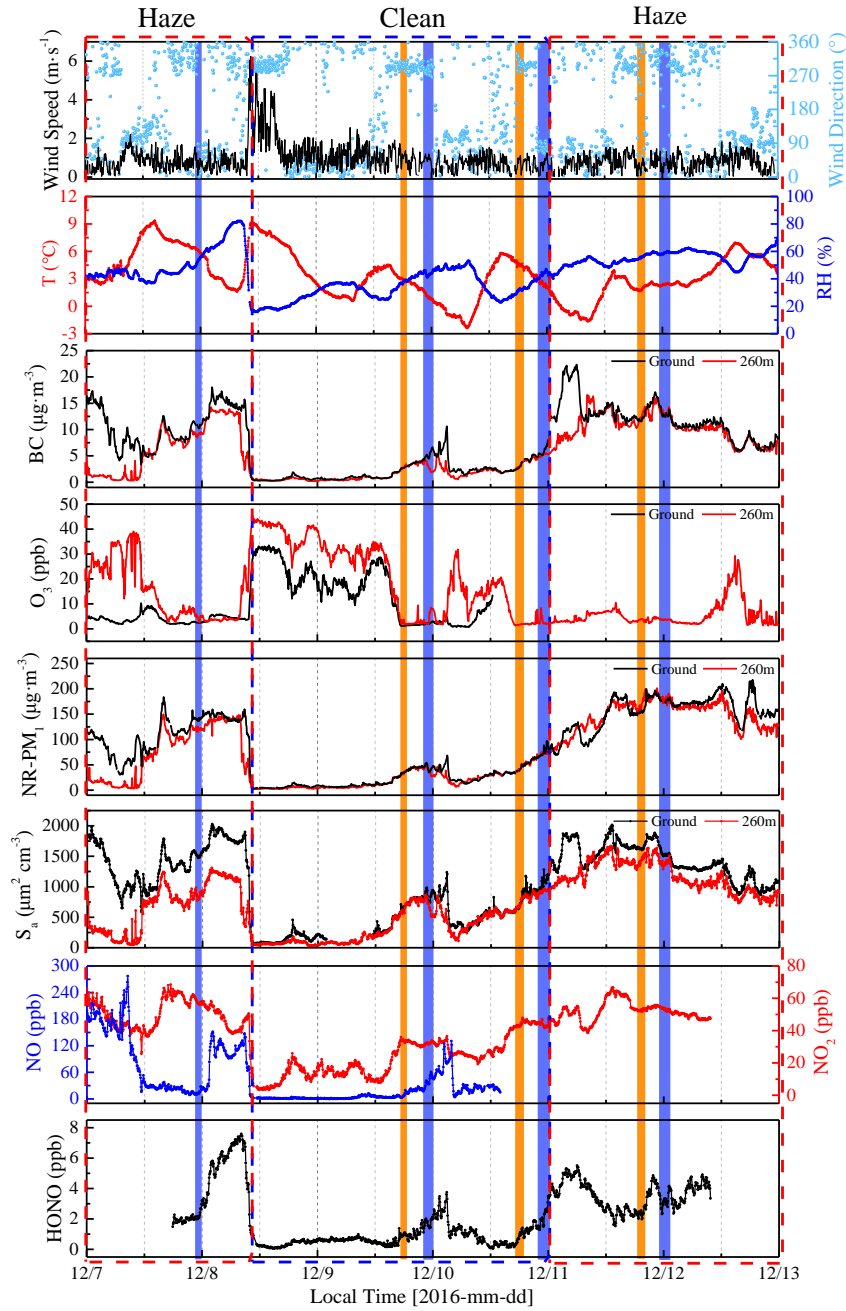


Figure 3. Time-series of wind speed (WS) and direction (WD), temperature (T), relative humidity (RH), BC, O_3 , NR- PM_{10} , aerosol surface area (S_a), NO, NO_2 , and HONO from December 7th to 12th 2016 at the IAP-Tower Division in Beijing, China. The shaded region represents the eight vertical measurements (Table S1). The orange shaded region represents the vertical measurements after sunset, and the violet shaded region represents the vertical measurements at night and midnight.

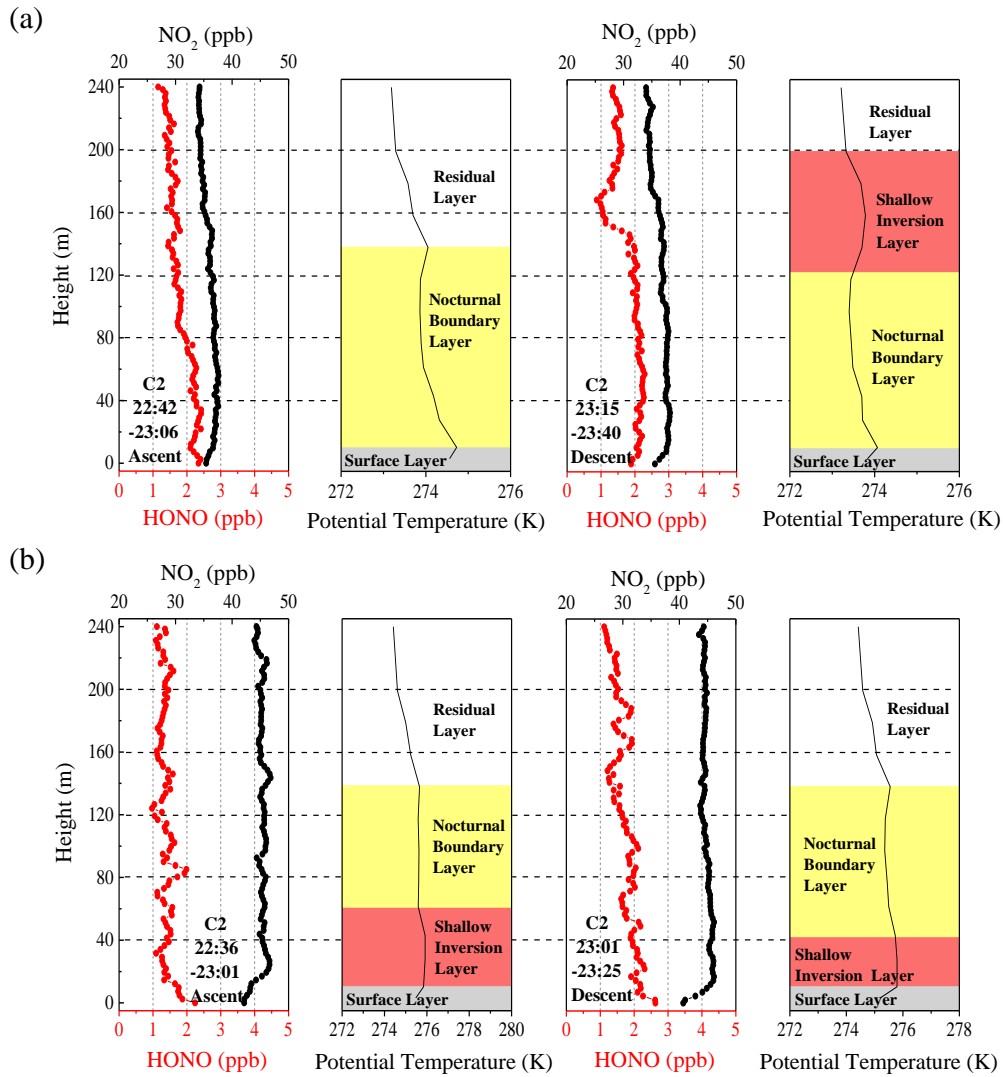


Figure 4. Nocturnal vertical profiles of HONO, NO₂, and the potential temperatures during the ascent and descent of the container on the (a) 9th and (b) 10th of December. The time in the figure corresponds to the measurement time of the vertical profile of the HONO and NO₂. The different colored shaded region indicates the nocturnal small-scale stratification (surface layer, nocturnal boundary layer, shallow inversion layer, and residual layer). The heights of the surface layer, the shallow inversion layer, the nocturnal boundary layer, and the residual layer are denoted by grey shaded regions, pink shaded regions, yellow shaded regions, and white shaded regions, respectively.

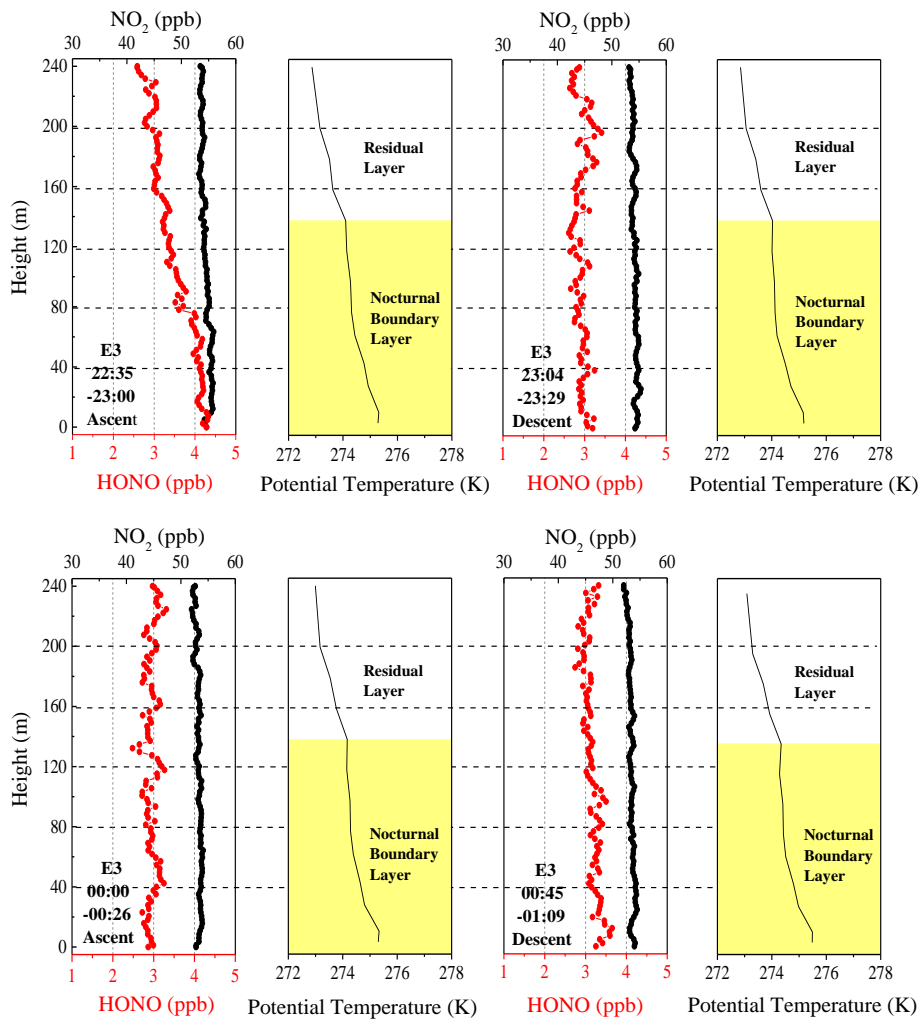


Figure 5. Vertical profiles of HONO and NO₂ on the night of December 11th and midnight of December 12th. The potential temperature profiles indicate nocturnal small-scale stratification (a nocturnal boundary layer and a residual layer). The height of the nocturnal boundary layer (NBL) is denoted by the yellow shaded region. The time in the figure corresponds to the measurement time of the vertical profiles of HONO and NO₂.

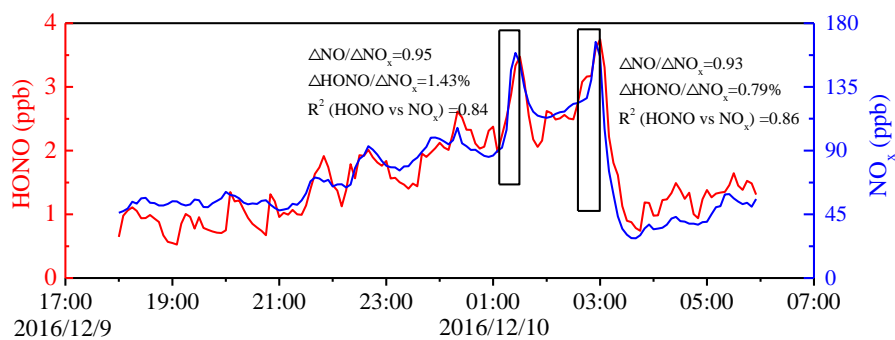


Figure 6. Temporal variation of nocturnal HONO and NO_x on December 9th to 10th, 2016. The HONO emission ratios were estimated using data collected in the black frame.

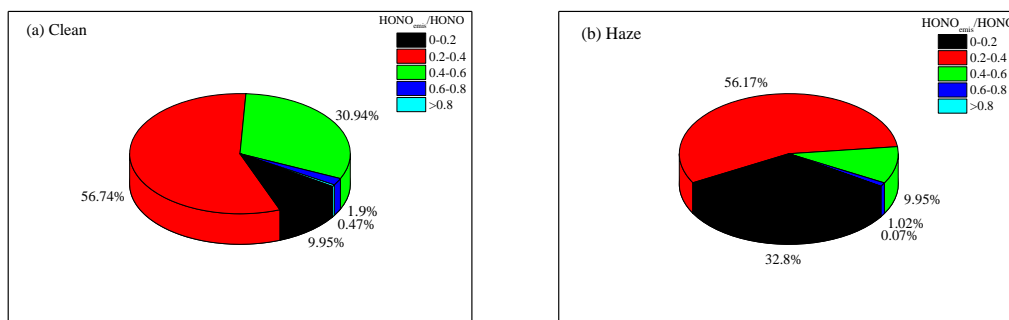


Figure 7. The nocturnal HONO_{emis}/HONO ratios frequency distribution during (a) clean and (b) haze episodes.

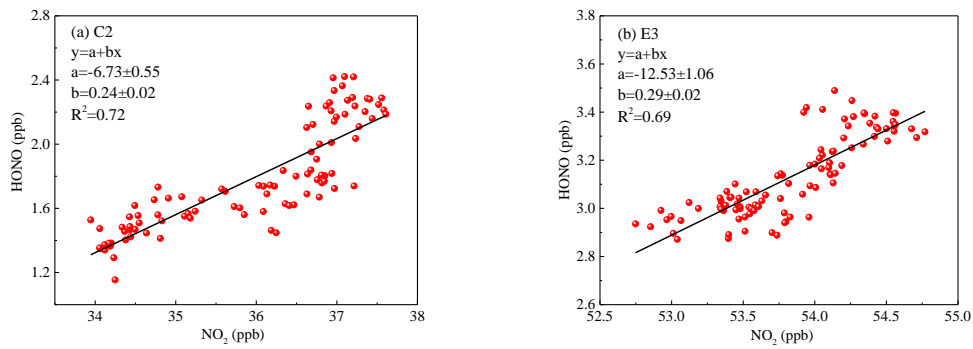


Figure 8. The correlation of the vertical profiles between HONO and NO₂ during (a) the clean episode (C2) and (b) the haze episode (E3) using a linear least squares regression fit.

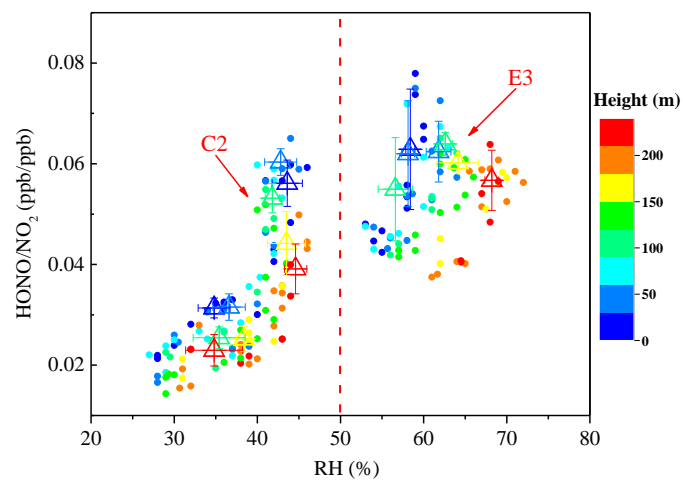


Figure 9. Scatter plot of HONO/NO₂ against RH of all vertical profiles during the clean episode (C2) and the haze episode (E3). The HONO/NO₂ ratio is color coded by the heights. Triangles are the average of the first five HONO/NO₂ values in each 10% RH interval at different height intervals (8–65 m, 65–120 m, 120–180 m, and 180–240 m).

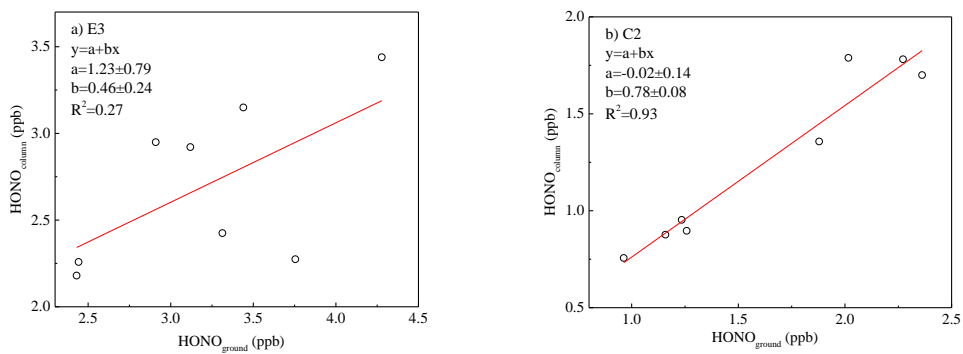


Figure 10. Orthogonal linear least squares correlation between the column average concentration of HONO (the average HONO column concentration from 10 to 240 m) and HONO measured from the ground level to 10 m above the ground level (AGL). Column values were calculated for-(a) E3 and (b) C2.

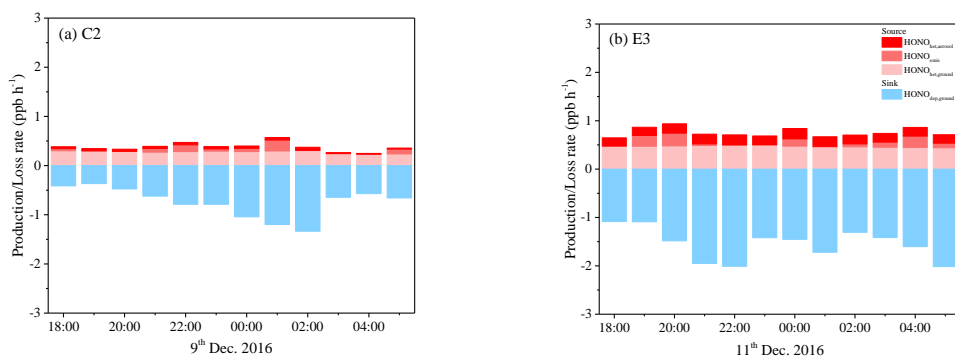


Figure 11. Separated contributions of production and loss terms (colored bars) of HONO on (a) the 9th (C2) and (b) 11th (E3) of December 2016. An upper limit uptake coefficient for NO₂ was adopted to calculate the HONO production rate on aerosol surface.